

# Chapter 4

## Experimental Results - Statistics

## 4.1 Overview

The present chapter includes a presentation and discussion of the results for two major geometries. For the first geometry, the swirler center-body takes the form of a cone and the nozzle flow is a simple swirling pipe flow with a free vortex center. In the second geometry, the swirler center-body has a cylinder attached that extends all the way through the nozzle to the sudden expansion interface between the nozzle and model combustor section. The resulting flow does not have a free vortex center and so is largely prevented from breaking down inside the nozzle as discussed in Section 4.3. The geometry with free vortex flow will be referred to as the "free vortex" geometry. The geometry with the center-body extending through the nozzle to the sudden expansion plane will be referred to as the "annulus" geometry. For each geometry, the mean and RMS flow profiles are presented.

The basic test matrix used for each geometry consists of two flow-rates and three swirl conditions. The two flow rates were chosen to be 50 SCFM and 100 SCFM, corresponding to Reynolds numbers of around 32,000 and 64,000 in the nozzle respectively (using  $D=2.9$  in). The experiments were limited to the 100 SCFM flow rate due to limitations in the building ventilation system and the inability to filter out a significant proportion of the olive oil seed. One of the swirl conditions is the zero swirl, plain jet flow condition. The other two swirl conditions depend on the nozzle geometry. The vane angles are much higher for the annulus nozzle case than for the free vortex case. Additional measurements at other swirl angles were also performed, but the data collected is not as detailed in terms of the number of downstream axial stations covered.

The coordinate system used has two anchors. The radial coordinate zero is the centerline of the test section. The axial coordinate zero is at the sudden expansion. Nozzle axial coordinates are therefore negative, and combustor axial coordinates are positive. The units of all coordinates are non-dimensionalized by the diameter of the nozzle,  $D_n$ , 2.9 inches (0.074 m) for the case of the free vortex geometry. Coordinates for the annulus nozzle geometry are non-dimensionalized by the difference between

the nozzle diameter and the center–body diameter,  $D_h$ , (2.9 - 1.0 = 1.9 inches).

The maximum swirl level studied in detail for the free vortex case is the largest swirl angle that did not produce a wake profile inside the nozzle. Large vane angles cause a vortex breakdown to occur immediately downstream of the cone center–body resulting in a wake type velocity profile inside the nozzle. This type of flow was studied by Dellenback et al. (1988) but has little practical relevance since the wake may support combustion resulting in flashback for an actual combustor exhibiting this type of flow field. Some measurements were performed at large vane angles inside the nozzle for completeness.

In the annulus geometry the maximum swirl angle studied in detail corresponds to a laminar swirl number of about 0.60 (Equation 3.5). The vane angle at which this swirl level was achieved is almost three times higher than the maximum angle used for the free vortex geometry.

A summary of the conditions studied is given in Table 4.1. The table identifies the geometry, the nominal air flow rate through the rig (i.e. not including seed flow air), the swirl condition and laminar swirl number. For the experiments reported here, the turbulent swirl number is never more than several percent from the laminar swirl number and therefore will not be reported separately. The table also gives the Reynolds number calculated based on the area mean velocity calculated for the geometry. The area mean velocity is reported in the last column of the table. The next to last column of the table reports the measured centerline of the flow. This measurement is only possible for the free vortex geometry when non-zero swirl exists. The centerline is the location where the mean swirl velocity crosses the zero axis. The location is interpolated from the two points lying on either side of the presumed vortex center. The value displayed in Table 4.1 is the deviation for a given condition from the average of all locations. The measurements show that the vortex center is measured consistently in the same location with deviations of less than one millimeter. As expected, the error is on the order of the extent of the LDV measurement volume in the radial direction ( $\sim 0.5mm$ ).

**Table 4.1:** Summary of experimental conditions studied in detail

Flow type	Nominal Q (SCFM)	Swirl	S	Re ( $\times 10^{-3}$ )	Center (mm)	Area mean U (m/sec)
Free vortex	50	Zero	–	34	–	5.8
Free vortex	50	Med	0.11	33	0.32	5.7
Free vortex	50	Max	0.21	34	-0.70	5.9
Free vortex	100	Zero	–	63	–	11.0
Free vortex	100	Med	0.12	63	0.32	11.0
Free vortex	100	Max	0.16	62	0.06	10.8
Annulus	50	Zero	–	25	–	6.51
Annulus	50	Med	0.28	25	–	6.52
Annulus	50	Max	0.60	23	–	6.00
Annulus	100	Zero	–	45	–	11.82
Annulus	100	Med	0.29	45	–	12.00
Annulus	100	Max	0.60	42	–	11.05

## 4.2 Free vortex geometry flow field

### 4.2.1 Nozzle flow field

Nozzle velocities were measured at  $x/D_n = -0.69$  and  $x/D_n = -0.35$ , just upstream of the sudden expansion. Figure 4.1 shows the axial and swirl velocity profiles for both axial locations for the medium swirl case at 50 SCFM nominal flow rate. Figure 4.2 shows the corresponding RMS velocity profiles. The  $\overline{u'w'}$  Reynolds stress is shown in Figure 4.3. Both the mean and RMS velocity profiles show that the flow evolution inside the nozzle is slow. The mean axial profiles exhibit a significant axial momentum surplus that appears to decay slowly as the sudden expansion is approached. The peak swirl velocity is also slightly decreasing lending support to the idea that the axial momentum surplus on the centerline is generated by the static pressure distribution experienced by the flow on the centerline. The static pressure distribution inside the flow is a strong function of the local swirl velocity distribution. As remarked by Garg and Leibovich (1979), the axial momentum surplus marks the approximate

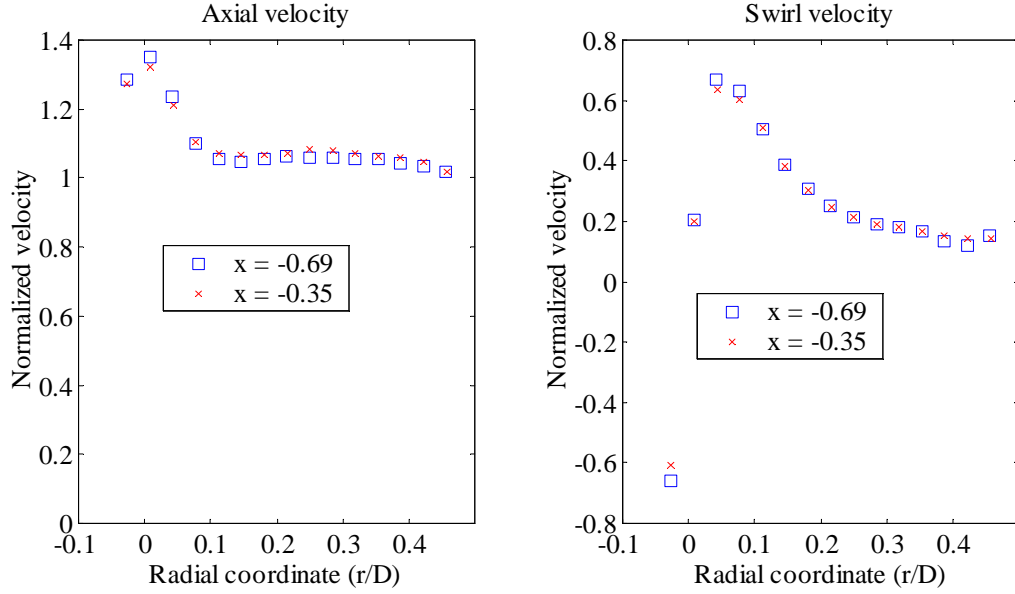


**Figure 4.1:** Comparison of nozzle mean velocity profiles at two axial locations for  $S=0.12$ ,  $Q=50$  SCFM

thickness of the vortex core. The distribution of swirl velocity in the vortex core causes a significant radial static pressure gradient in this area. Near the formation of the vortex, immediately downstream of the cone, the core is the thinnest and the axial momentum has the largest surplus at the centerline. Downstream, due to the shear present constantly in the flow, the swirl momentum is dissipated slowly and the flow actually decelerates on the axis. The turbulence production through swirl can be seen relatively easily in the outer parts of the flow when examining Figure 4.2.

The hypothesis that the swirl velocity distribution causes the axial momentum surplus is supported by the results shown in Figure 4.4 which plots the mean velocity distributions for all three main swirl conditions tested at  $x/D_n = -0.35$ . The corresponding RMS and  $\overline{u'w'}$  stress plots are shown in Figures 4.5 and 4.6 respectively. The zero swirl case actually shows a slight axial momentum deficit in the center of the flow. The wake is caused by the cone center-body. The wake is not observed for the swirl cases because the static pressure gradient along the centerline is such that at the formation of the vortex, the flow actually accelerates at the centerline. Fur-

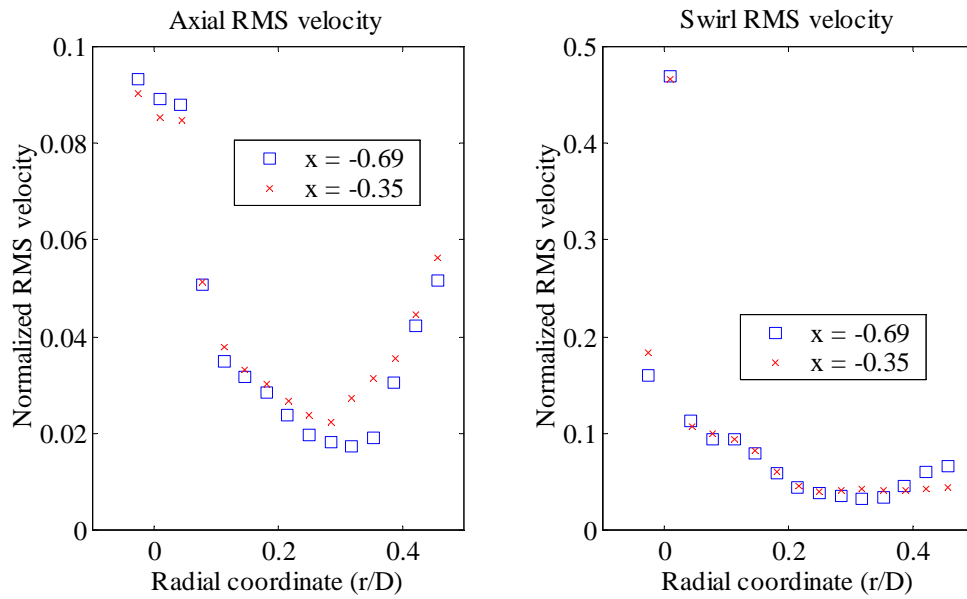


**Figure 4.2:** Comparison of nozzle RMS velocity profiles at two axial locations for  $S=0.12$ ,  $Q=50$  SCFM

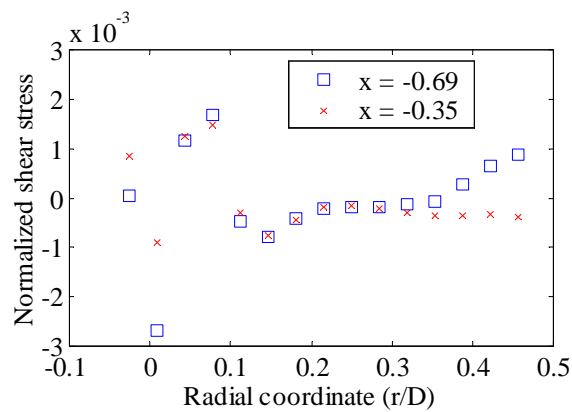


**Figure 4.3:** Comparison of nozzle  $\overline{uw}$  stress profiles at two axial locations for  $S=0.12$ ,  $Q=50$  SCFM

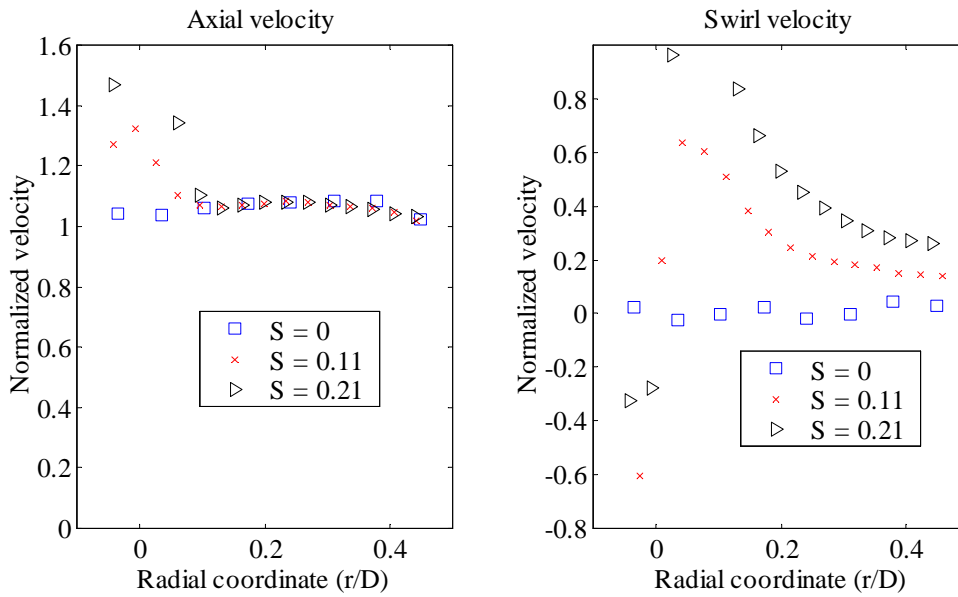


**Figure 4.4:** Comparison of nozzle mean velocity profiles for all swirl conditions at  $x/D_n = -0.35$  and  $Q = 50$  SCFM

ther supporting the hypothesis, Figure 4.4 shows that the axial momentum surplus is directly proportional to the level of swirl. Consistent with the work of Garg and Leibovich (1979), the vortex core (as marked by the width of the axial momentum surplus) is increasing with increasing swirl. However, the linear region of swirl does not change significantly for each of the conditions. It is possible that the wider axial momentum surplus is simply a result of momentum diffusion away from the centerline. The turbulent transport of momentum is enhanced by the high concentration of turbulent energy near the centerline of the flow. The axial RMS velocity is only moderate but the swirl RMS velocity is very high.

The high RMS velocity measured in the center of the flow is caused by the turbulent movement of the vortex core around the centerline of the flow. With increasing swirl levels, the core of the flow contains less and less olive oil seed. When the pipe sections in the nozzle are removed and replaced by a large window, the LDV laser beams illuminate the turbulent motion of the core, which are of a time scale slow enough to capture with the unaided eye. The absence of seed at the center of the

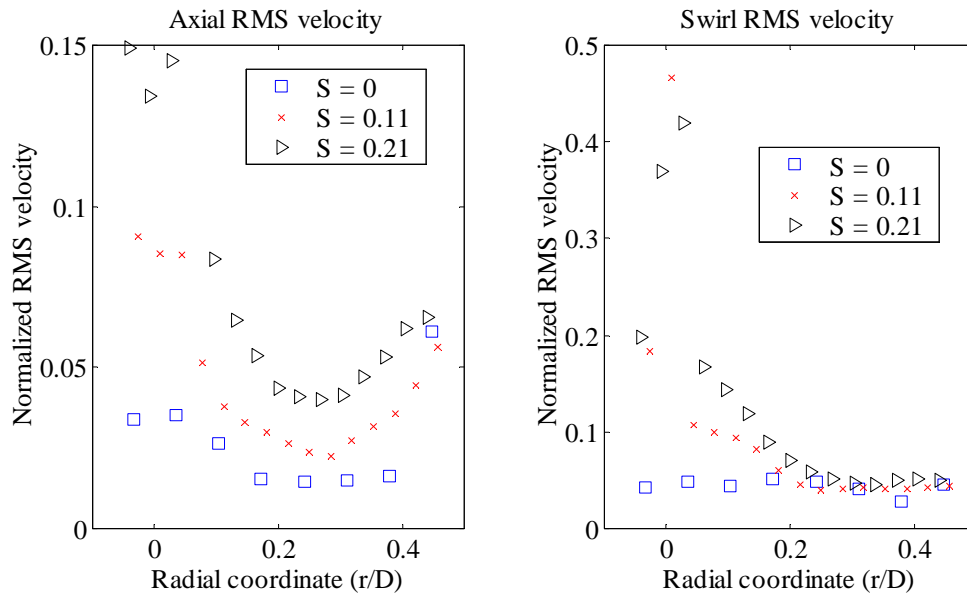


**Figure 4.5:** Comparison of nozzle RMS velocity profiles for all swirl conditions at  $x/D_n = -0.35$  and  $Q = 50$  SCFM

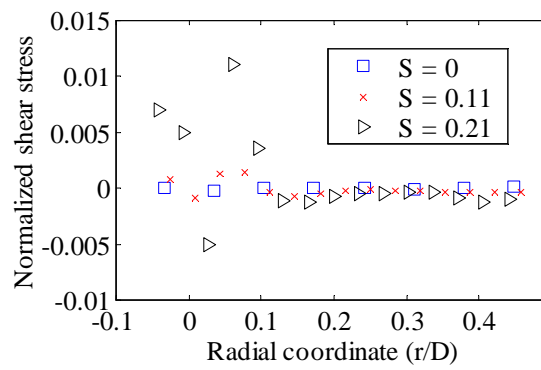


**Figure 4.6:** Comparison of nozzle  $\overline{uw}$  stress profiles for all swirl conditions at  $x/D_n = -0.35$  and  $Q = 50$  SCFM



nozzle also causes difficulties in data collection for that region. Although reliable velocity statistics can be reported for this region, the calculation of power spectra is hampered significantly by low data rates (20-100 Hz). Power spectra will be examined in detail in Chapter 5.

One of the features most important to computational modeling of swirling flows is also apparent from Figure 4.5. With increasing swirl level, the turbulence in the flow becomes less and less isotropic and more and more non-uniform. Note that even for the case without swirl, the turbulence is non-uniform, although nearly isotropic due to the wake generated turbulence located found at the center of the flow.

The shear stress distribution shown in Figure 4.6 looks somewhat indecipherable at first glance. The distribution must however obey certain rules of symmetry and these help in the interpretation. The LDV probe measures radial velocity fluctuations at the center line and the  $\overline{uv}$  stress must be anti-symmetric about the centerline for the flow to be axisymmetric. Outside the very center of the flow  $\overline{u'w'}$  stresses are zero for axisymmetric flows in the absence of swirl. The  $\overline{u'w'}$  stress distribution should be anti-symmetric about the centerline of the flow. Some useful information can now be extracted from the data. The shear stress is essentially zero outside of the vortex core and for the zero swirl case, as expected. In this region, the turbulence is also closest to isotropic. The magnitude of the shear stress increases significantly with swirl at the centerline of the flow where the highest discrepancy is found between axial and swirl RMS velocity. For both medium and maximum swirl conditions, the  $\overline{u'w'}$  stress appears to change sign across the centerline of the flow, which is required by anti-symmetry. The high shear stress amplitudes are associated with rapid redistribution of mean momentum and turbulence production.

The distribution of shear stress shown in Figure 4.6 must also be viewed critically due to the resolution limitations of the LDV. The LDV probe volume has a length of 0.45 mm and is oriented parallel to the radial direction of the flow field. The LDV thus has difficulty measuring the highly irregular shear stress function near the centerline of the flow. Nevertheless, the distributions measured for both swirl cases are similar, even though the larger swirl case has a much higher shear stress amplitude. The large

maxima obtained immediately outside of the core are not able to be resolved in the present measurements. The separation from edge of probe volume to edge of probe volume for the displayed points is equal to four probe volume lengths. A finer mesh of collected data points may improve on the details of the measured distribution, but the accuracy of the measured shear stress distribution will remain questionable.

The results for the medium swirl case ( $S=0.12$ ) for the two flow rates studied are compared in Figures 4.7 to 4.9. Figure 4.7 shows the normalized mean velocity profiles measured. The distributions are very similar. The vane angle used for both conditions is the same and the similarity is expected. A curious feature of the higher flow rate results is the dent in the axial momentum surplus at the centerline of the flow. Figure 4.8 shows that the sudden deficit also causes a large jump in the axial RMS velocity. Figure 4.10 shows the histogram of the velocities measured. A large maximum in the distribution occurs near the expected mean of the velocity, based on the lower flow rate results. In addition however, a number of data points fall between 0 and 0.5, giving a bimodal character to the velocity distribution. The intermittent low velocity is caused by the sporadic upstream movement of the vortex breakdown zone from the sudden expansion into the nozzle.

The vortex core size does not appear to be a function of flow rate. The lack of increase in the vortex core size exacerbates the low seed condition at the vortex centerline. Even though the same number of bursts were collected at each flow rate, the number of data points validated for the lower flow rate is about double that validated at the high flow rate. Although the centerline location is the only location where a bimodal histogram can be found, the effects of the intermittency can still be seen for the surrounding points. The axial RMS velocity is elevated above that of the lower flow rate for over half the radius. The shear stress distribution shown in Figure 4.9 also exhibits a large peak near the center line, associated with the intermittency discussed above.

Figures 4.11 to 4.13 display a comparison between the results of the two non-zero swirl levels studied at 100 SCFM. The vane angle used for the maximum swirl condition at 100 SCFM is not equal to that used for 50 SCFM. Using the same

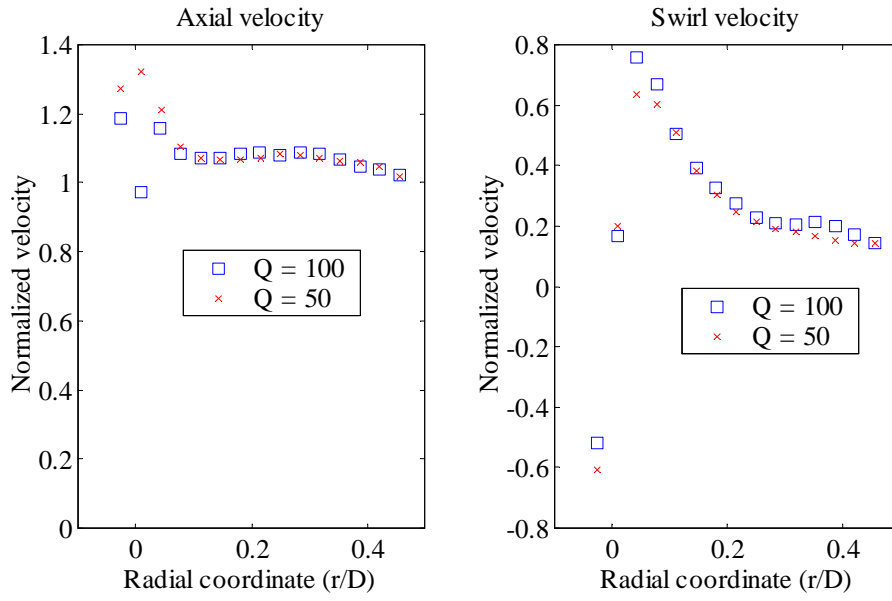


**Figure 4.7:** Comparison of nozzle mean velocity profiles at both flow rates for  $S=0.12$  at  $x/D_n=-0.35$

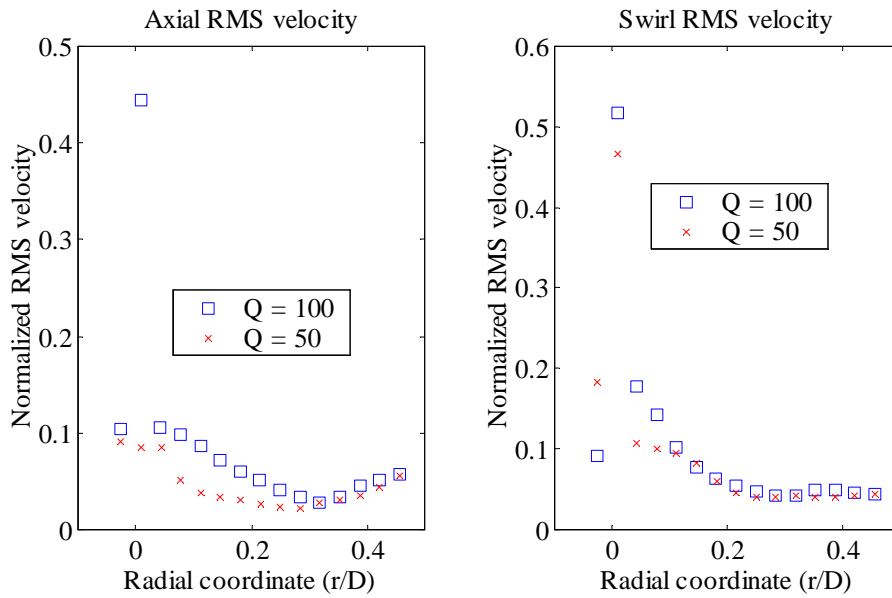


**Figure 4.8:** Comparison of nozzle RMS velocity profiles at both flow rates for  $S=0.12$  at  $x/D_n=-0.35$

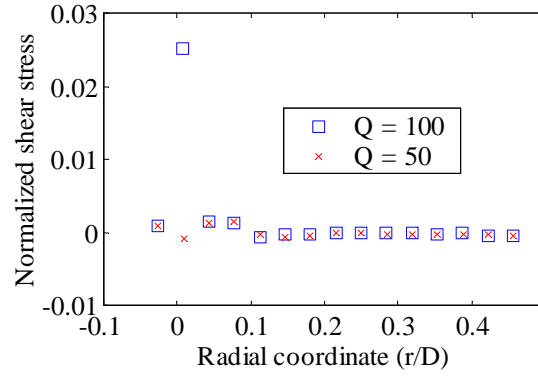


**Figure 4.9:** Comparison of nozzle  $\overline{uw}$  stress profiles at both flow rates for  $S=0.12$  at  $x/D_n=-0.35$

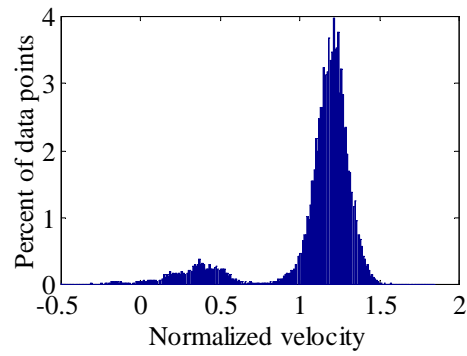


**Figure 4.10:** Histogram of axial velocities at the centerline for  $x/D_n=-0.35$ ,  $Q=100$  SCFM and  $S=0.12$

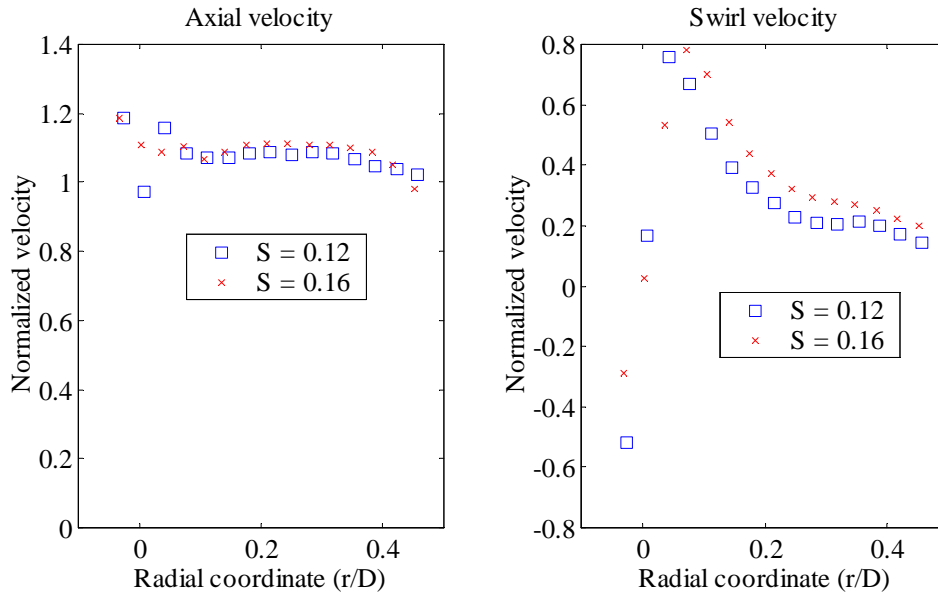


**Figure 4.11:** Comparison of nozzle mean velocity profiles at two swirl levels ( $S=0.12,0.16$ ) for  $Q=100$  SCFM at  $x/D_n=-0.35$

vane angle resulted in a wake type profile inside the nozzle, indicating that vortex breakdown had moved into the nozzle and upstream to the cone center-body. The swirl angle used for the maximum swirl condition at 100 SCFM was chosen such that the velocity profile did not exhibit a true wake profile. Figure 4.11 shows that the dent in the axial momentum surplus discussed above has expanded for the higher swirl condition.

An examination of the histograms of axial velocity support the notion that the lack of a pronounced axial momentum surplus is due to the breakdown moving into the nozzle intermittently. Figure 4.14 shows the histogram of axial velocities at the position closest to the centerline for the maximum swirl condition at 100 SCFM. The distribution is again bi-modal and the amount of data contained in the main distribution maximum is lower compared to the lower swirl level. The results indicate that the breakdown moves into the nozzle more often under these conditions. The extent of the bi-modal distribution has also increased for the higher swirl case. The location next to the centerline location also exhibits a slight bi-modal distribution. The RMS

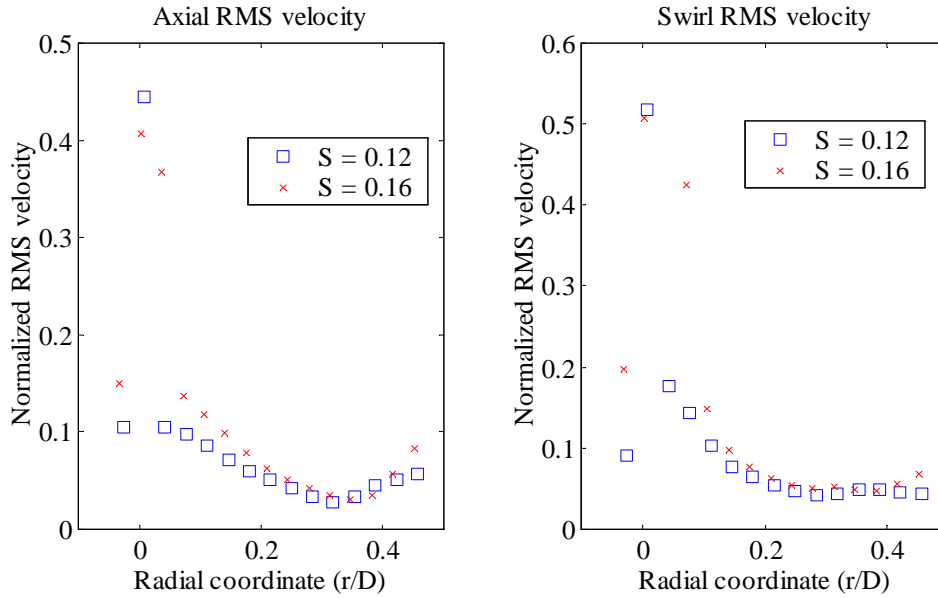


**Figure 4.12:** Comparison of nozzle RMS velocity profiles at two swirl levels ( $S=0.12, 0.16$ ) for  $Q=100$  SCFM at  $x/D_n=-0.35$

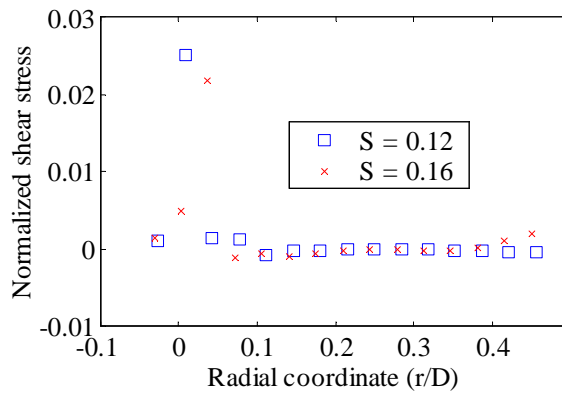


**Figure 4.13:** Comparison of nozzle  $\overline{w\overline{w}}$  stress profiles at two swirl levels ( $S=0.12, 0.16$ ) for  $Q=100$  SCFM at  $x/D_n=-0.35$

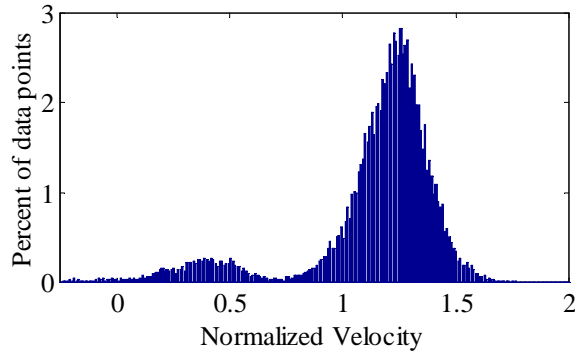


**Figure 4.14:** Histogram of axial velocities at the centerline for  $x/D_n=-0.35$ ,  $Q=100$  SCFM and  $S=0.16$

values plotted in Figure 4.12 also show the influence of the bi-modal distribution. The area of very high axial RMS velocity has increased. The swirl RMS velocity at the same radial locations has also increased. The maximum mean swirl velocity achieved for the maximum swirl case is very close to the lower swirl case. The RMS value at the same point however is much higher. Figure 4.15 shows the histogram of swirl velocities at this location. The distribution is very wide and is difficult to characterize. The maximum of the distribution is near a non-dimensional velocity of one which would cause the mean swirl velocity profile shown in Figure 4.11 to have a maximum above that of the lower swirl case. Two events are responsible for the distribution shown in Figure 4.15. The first event is the movement of breakdown zone upstream which at the affected points reduces the local swirl velocity. The second event is the movement of the vortex core, which increases with increasing flow rate. The movement of the core also introduces lower velocities and further fills in the distribution below the main peak in the distribution at a non-dimensional velocity of 1.

The data has thus shown that even though the nozzle Reynolds numbers are relatively high, the flow behaves very differently for the two flow rates studied. The core remains intact up to a swirl number of 0.21 at a flow-rate of 50 SCFM whereas at 100 SCFM, it is impossible to achieve swirl numbers at the nozzle exit above 0.16.

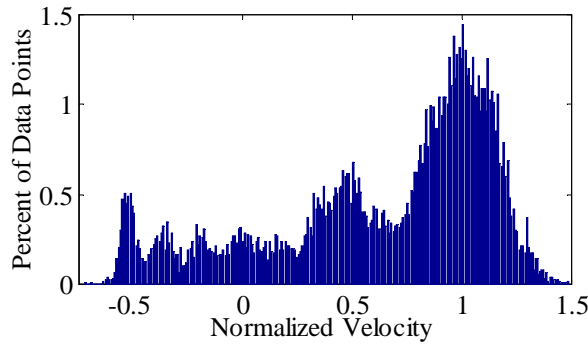


**Figure 4.15:** Histogram of swirl velocities outside centerline for  $x/D_n = -0.35$ ,  $Q=100$  SCFM and  $S=0.16$

One of the main differences between the two flows is the amount of turbulence present and associated turbulent transport. Since the vortex core size appears nearly constant between the two flow rates, the shear in the flow is higher along with the associated turbulence production. The increase of turbulent energy inside the core causes erratic motion of the core which eventually and, depending on the condition, intermittently destabilizes the flow. The matter of stability will be further addressed in Chapter 5.

## 4.2.2 Post sudden expansion flow field

Velocities were measured at five axial locations downstream of the sudden expansion. The first location measured is  $x/D_n = 0.44$ . For this axial location it is possible to perform measurements to  $r/D_n = -0.17$ . The other four axial measurement locations are  $x/D_n = 0.97, 1.48, 2$  and  $3.14$  (non-dimensionalized by diameter). The extent of measurements thus does not cover the entire redevelopment region of the flow field. However, the measured axial locations cover the dynamically critical and interesting parts of the flow field. The mean and RMS velocities are normalized by the area mean velocity calculated for the  $x/D_n = -0.35$  nozzle location. The  $\overline{u'w'}$  stress is normalized by the square of the area mean velocity. The velocities are given in Table 4.1. The radial extent of the combustor test section in normalized coordinates is from  $r/D_n = -1.25$  to  $1.25$ .



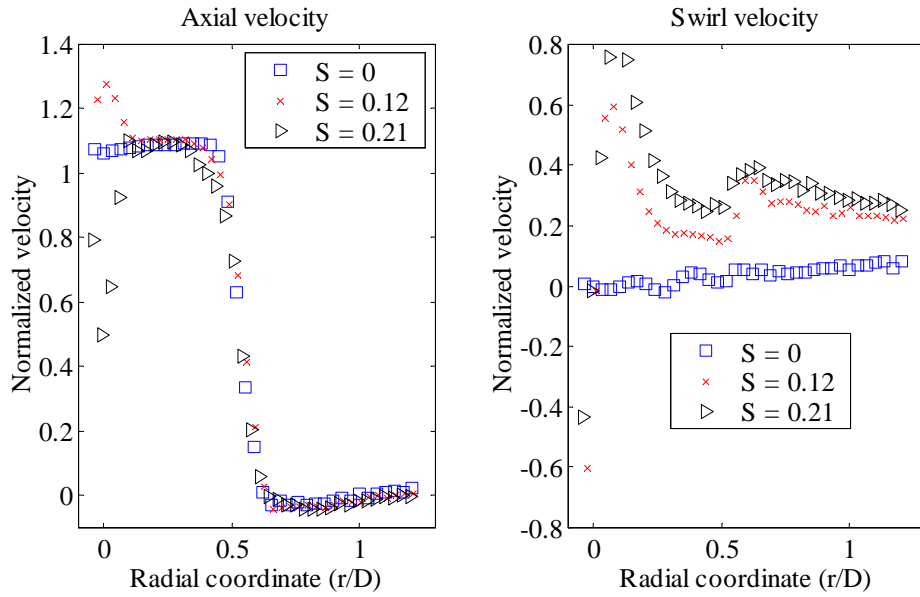


**Figure 4.16:** Comparison of combustor mean velocity profiles at all swirl levels for  $Q=50$  SCFM at  $x/D_n=0.44$

Figure 4.16 shows the results obtained at all three swirl levels studied for the low flow rate of 50 SCFM. The axial location of measurement is  $x/D_n=0.44$ . Especially the swirl profiles do not show a large difference in comparison to the last measured nozzle station. The axial velocities, however show more significant changes depending on the level of swirl. With no swirl and the intermediate amount of swirl, the axial flow profiles still resemble those encountered in the nozzle. The intermediate axial flow profile still exhibits a small axial momentum surplus on the centerline. The maximum swirl level axial velocity profile however exhibits a sharp wake in the center of the flow, whose width is about equal to the original vortex core. It is interesting to note that the mean swirl velocity profile shows little effect of this drastic change in the axial velocity profile. The RMS velocity profiles, shown in Figure 4.17 however are clearly influenced by this change.

Both swirl and axial velocity profiles show two large maxima. The maximum near the centerline of the flow is a strong function of the swirl condition. The maximum is virtually absent for the no swirl case and becomes stronger as swirl is increased.

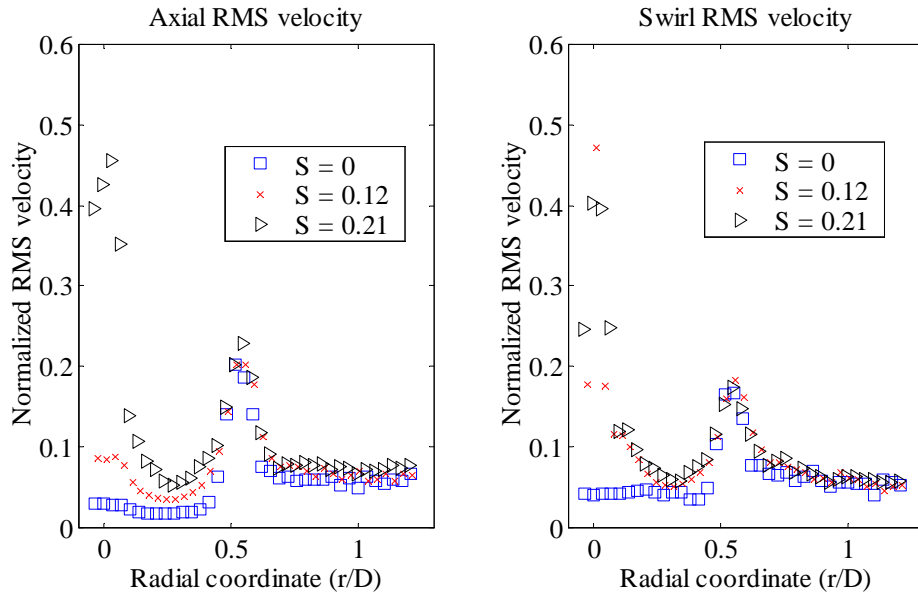


**Figure 4.17:** Comparison of combustor RMS velocity profiles at all swirl levels for  $Q=50$  SCFM at  $x/D_n=0.44$

In contrast to this the RMS velocity maxima in the outer shear layer are virtually constant for all levels of swirl. In comparing the results of Figure 4.17 to Figure 4.4, it becomes apparent that the centerline maximum of swirl RMS velocity has only changed very little whereas the energy in the axial RMS velocity has more than doubled. A similar energy gain appears to have occurred for the RMS velocity near the wall of the nozzle.

The massive redistribution of mean momentum and generation of turbulent energy at the flow centerline at the high swirl level requires an efficient mechanism. One of the catalysts in the production of turbulence and redistribution of mean momentum is the turbulent shear stress  $\overline{uw}$ , which is shown in Figure 4.18. The large peaks near the centerline indicate the high level of dynamic activity in the flow. The center shear stress dwarfs the small undulations of shear stress experienced by the flow at the outer shear layer. These small undulations are again proportional to the swirl strength and the shear stress is virtually zero in the no swirl case, which is not surprising considering the underlying turbulent state is relatively close to isotropic.

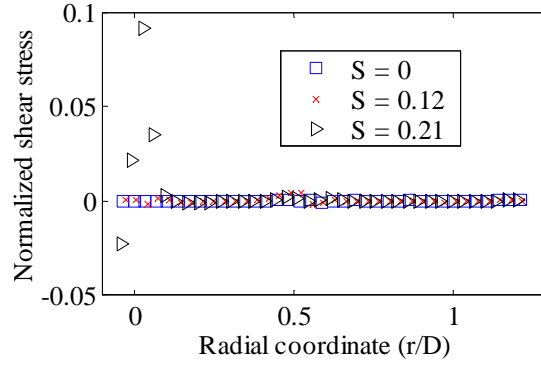


**Figure 4.18:** Comparison of combustor  $\overline{u'w'}$  stress at all swirl levels for  $Q=50$  SCFM at  $x/D_n=0.44$

Figures 4.19 to 4.21 show the evolution of the flow field in the absence of swirl at a nominal flow rate of 50 SCFM. The axial velocity maximum at the center of flow does not exhibit any decrease, even at  $x/D_n=3.14$ . The swirl velocity is essentially zero throughout the flow field. The  $\overline{u'w'}$  shear stress shown in Figure 4.21 is also very small. The only appreciable deflections from zero stress occur near the outer shear layer. The small  $\overline{u'w'}$  shear stress is consistent with the near isotropic conditions in the flow field. Both axial and swirl RMS velocities, shown in Figure 4.20 increase downstream.

The location of maximum RMS velocity is constant as the flow develops. The maximum axial RMS velocity along the radius increases slightly as the flow develops. The swirl RMS velocity maximum stays nearly constant. Both RMS velocity distributions widen as the shear layer grows in the down stream direction. The widths of the RMS velocity distributions are consistent with the increase in the shear layer thickness seen in the development of the axial velocity profiles.

Figures 4.22 to 4.24 describe the evolution of the flow field downstream for the medium swirl case ( $S=0.12$ ). The velocity surplus that persisted to  $x/D_n=0.44$  is still present at  $x/D_n=0.97$ . Further downstream however, the momentum surplus is gone and the axial momentum spreads relatively quickly. The centerline maximum velocity decreases by 40% over two nozzle diameters. At the same time, the azimuthal

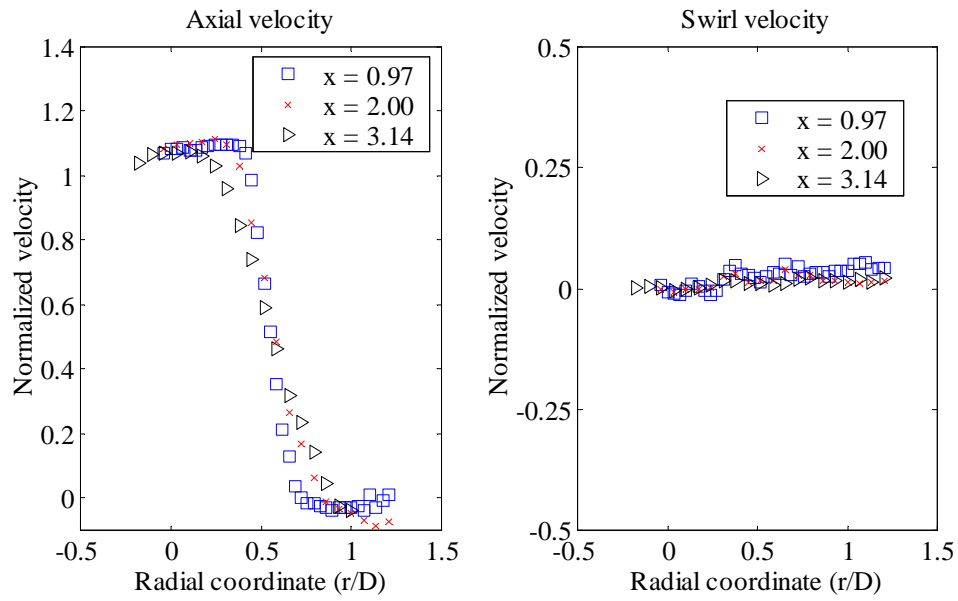


**Figure 4.19:** Evolution of combustor mean velocity profiles for  $S=0$ ,  $Q=50$  SCFM

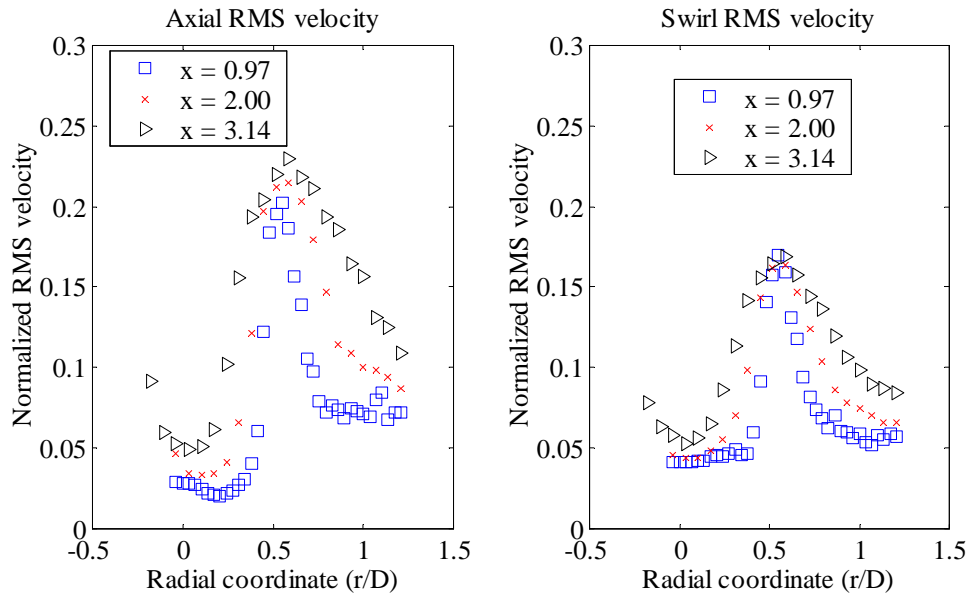


**Figure 4.20:** Evolution of combustor RMS velocity profiles for  $S=0$ ,  $Q=50$  SCFM

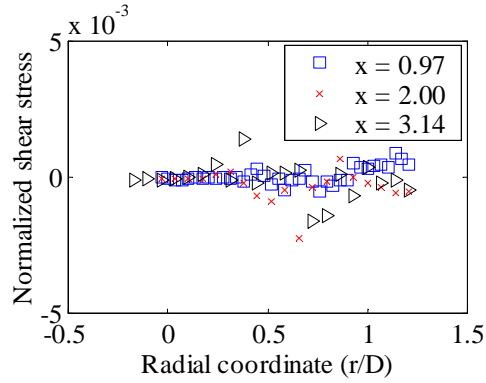


**Figure 4.21:** Evolution of combustor  $\overline{uw}$  stress profiles for  $S=0$ ,  $Q=50$  SCFM

momentum is almost entirely dissipated. At the last station measured, a very shallow solid body rotation type profile shows the start of the formation of a new very wide vortex core. The speed of development of this swirling flow with a relatively small swirl number of 0.12 stands in strong contrast to the zero swirl condition just discussed, where the axial velocity maximum had not yet decreased at all from its nozzle maximum.

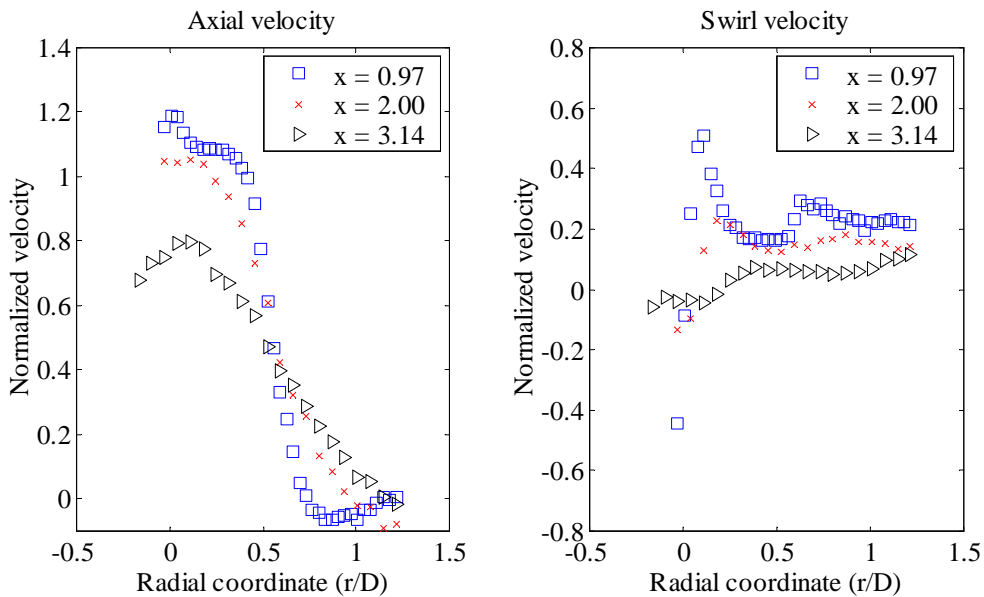


**Figure 4.22:** Evolution of combustor mean velocity profiles for  $S=0.12$ ,  $Q=50$  SCFM

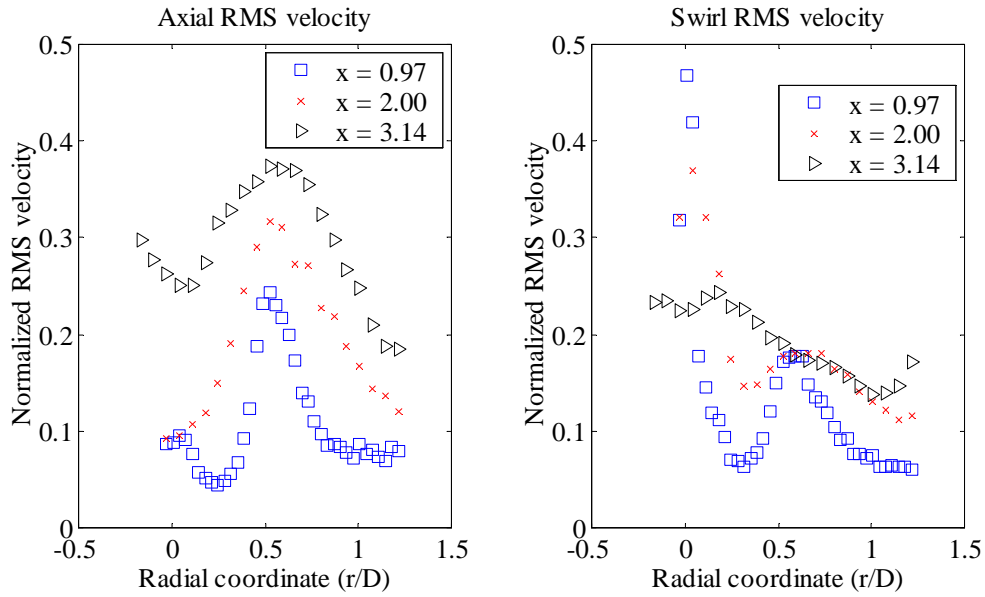


**Figure 4.23:** Evolution of combustor RMS velocity profiles for  $S=0.12$ ,  $Q=50$  SCFM

The RMS velocity maximum at the centerline is overtaken by the growth and spread of turbulent energy from the outer shear layer. At the last station measured, an axial RMS velocity minimum is actually seen at the centerline (Figure 4.23). The significant swirl RMS velocity maximum at the centerline, loses its sharp character downstream. The swirl RMS velocity distribution does not exhibit the same outer shear layer maximum. Whereas the RMS velocity levels at the centerline have almost equalized at  $x/D_n=3.14$ , the outer shear layer region continues to exhibit a high degree of anisotropy, consistent with the continuation of turbulent energy production. Overall, the RMS velocities measured are extremely high and considering the local mean velocities, show that flow reversal occurs intermittently almost all along the combustor radius at  $x/D_n=3.14$ . The high RMS velocities also contribute to the relatively non-smooth velocity profiles. Each data point consists of an average of approximately 150,000 points, but due to the high RMS velocities it is difficult to reduce the variance in the estimate of the mean.

Figure 4.24 shows the evolution of the turbulent  $\overline{u'w'}$  shear stress. The maxima and minima of the flow field increase downstream. This behavior is consistent with

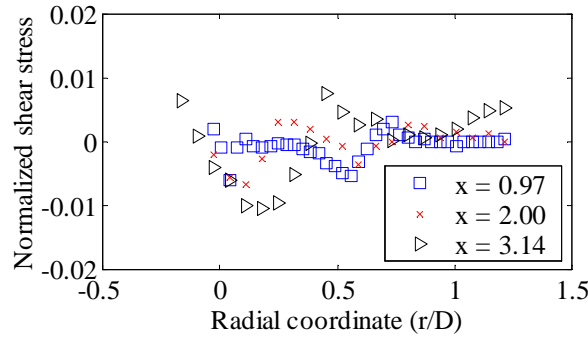


**Figure 4.24:** Evolution of combustor  $\overline{u'w'}$  stress profiles for  $S=0.12$ ,  $Q=50$  SCFM

the large amount of turbulent energy production and mean momentum redistribution and dissipation experienced by the flow as it develops downstream. The turbulence production term associated with the  $\overline{u'w'}$  shear stress term is  $-\overline{u'w'}\partial W/\partial x$ . It is unlikely that this production term is a major contributor to the production of turbulent kinetic energy. Considering however that the swirl distribution is decreasing axially, areas of positive turbulent shear stress will contribute to the production of turbulent kinetic energy whereas negative turbulent shear stress will contribute to the destruction of turbulent kinetic energy, returning the energy back to the mean flow.

Figures 4.25 to 4.27 show the evolution of the flow field for the  $S=0.21$  swirl condition at 50 SCFM nominal air flow. The velocity deficit at the center of the flow is dissipated very rapidly as may be expected considering how thin the initial wake was. The initial size of the wake is around  $1/10 D$  so that traveling one nozzle diameter downstream, is equivalent to ten wake widths. This distance is very large, especially considering the high amount of turbulence present in the flow which will enhance the momentum exchange between the high and low velocity region. Note that the  $\overline{u'w'}$  shear stress shown in Figure 4.27 exhibits a large maximum near the center of the flow, supporting the idea of enhanced mixing by turbulent kinetic energy production and transport. Overall, the flow for the higher swirl number develops even more quickly than for  $S=0.12$ . The turbulence levels at the last measured axial station, are lower for the  $S=0.21$  case than the  $S=0.12$  case. However, at  $x/D_n=2$  the turbulence

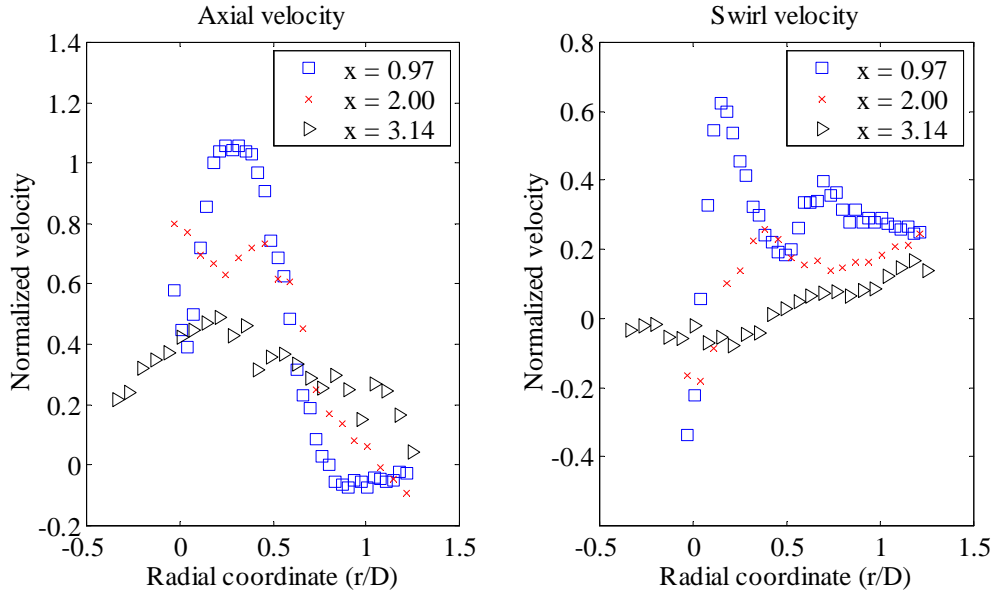


**Figure 4.25:** Evolution of combustor mean velocity profiles for  $S=0.21$ ,  $Q=50$  SCFM

levels at  $S=0.21$  exceed those at  $S=0.12$ . The production of turbulence thus is higher earlier in the flow for the higher swirl case. Again consistent with this picture is the rapid dissipation of azimuthal momentum. The maximum swirl velocity for the  $S=0.21$  case starts out 20% above that for  $S=0.12$ . At  $x/D_n=2$ , the two maxima are however almost equal. The rapid decrease in azimuthal momentum may also play a major role in causing the initial wake profile on the flow centerline. The rapid change in the distribution of azimuthal momentum causes an increase of the adverse pressure gradient experienced by the flow as it enters the sudden expansion.

The RMS velocity profiles shown in Figure 4.26 also show evidence of the more rapid development. The two axial RMS velocity peaks merge downstream and result in a relatively flat profile of RMS velocity at  $x/D_n=3.14$ . The swirl RMS velocity profile at  $S=0.21$  behaves very similarly to the swirl RMS velocity profile at  $S=0.12$ . The inner swirl RMS velocity maximum is consumed quickly and little RMS velocity gain occurs outside the center of the flow. The fact that the swirl RMS velocity remains nearly constant downstream, again gives rise to a significant amount of anisotropy in this region, although the anisotropy is lower at  $x/D_n=3.14$  for the



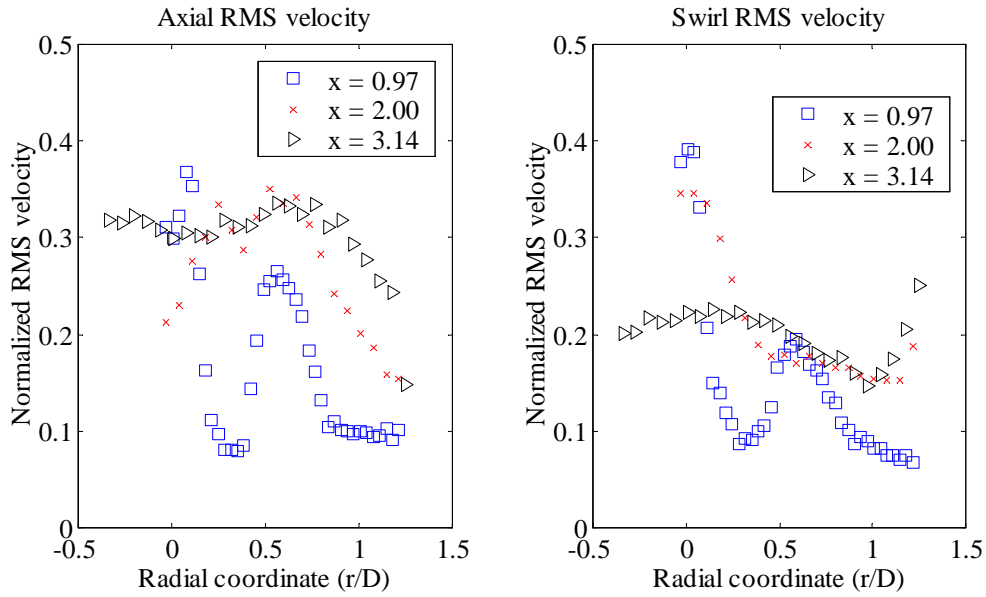


**Figure 4.26:** Evolution of combustor RMS velocity profiles for  $S=0.21$ ,  $Q=50$  SCFM

$S=0.21$  case because the significant maximum in axial RMS velocity seen for the  $S=0.12$  case is absent for the  $S=0.21$  case. Based on the fact that the swirl RMS velocity is relatively constant in the outer shear layer, it is possible to hypothesize that the major influence of swirl on the flow field development is due to its influence on the local static pressure distribution and in turn then on the axial velocity distribution. Swirl appears less important in affecting the outer shear layer dynamics.

The accelerated development of the flow is also underlined by the  $\overline{u'w'}$  shear stress distribution shown in Figure 4.27. The large amplitude seen for the  $S=0.12$  case at  $x/D_n=3.14$  is absent. Instead, the  $x/D_n=0.97$  location exhibits the highest shear stress.

Figure 4.25 shows a slight asymmetry, especially in the axial velocity profile at  $x/D_n=3.14$ . The asymmetry observed may or may not be real because of the uncertainty associated with the measurement of the mean velocity in this region of extremely high turbulence. The asymmetry can also be deduced from the  $\overline{u'w'}$  shear stress distribution shown in Figure 4.27. The distribution does go to zero near the centerline, but the stresses do not have the anti-symmetry about the centerline

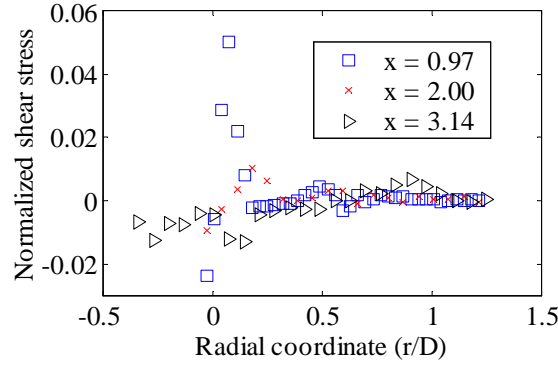


**Figure 4.27:** Evolution of combustor  $\overline{uw}$  stress profiles for  $S=0.21$ ,  $Q=50$  SCFM

required for axisymmetric flow. A much more significant asymmetry of the flow field was measured under the same conditions with the pipe sections replaced by a large window. Originally, the experiments were to be performed with the large windows in place. The pipe sections, that maintain the pipe curvature were found necessary only after the measurements at  $S=0.21$  at 50 SCFM had been performed. The asymmetry observed in the flow field is shown clearly in Figure 4.28. Almost the entire window side half of the test section contains time-mean reverse flow. All other possible causes for the asymmetry were eliminated before replacing the large window with the pipe section elements. Only then was the asymmetry essentially absent. The asymmetry was not only present at this axial location but gradually develops from the point the flow exits the nozzle. This involuntary experience in flow control shows how sensitive swirling flows are to their geometry and how minor geometrical changes can have a global influence on the flow field. The very same high sensitivity also makes swirling flows so attractive for the application of flow control.

Figures 4.29 to 4.31 show the velocity profiles at  $x/D_n=0.44$  for all three swirl conditions studied at 100 SCFM. The results for zero swirl and  $S=0.12$  are very similar to the results for the corresponding conditions at 50 SCFM. The  $S=0.12$  case shows a small axial momentum surplus at the center line. The zero swirl case exhibits an essentially flat axial velocity profile at the center of the tube. The mean velocity for the maximum swirl case shows a small local minimum in the pipe center. The swirl

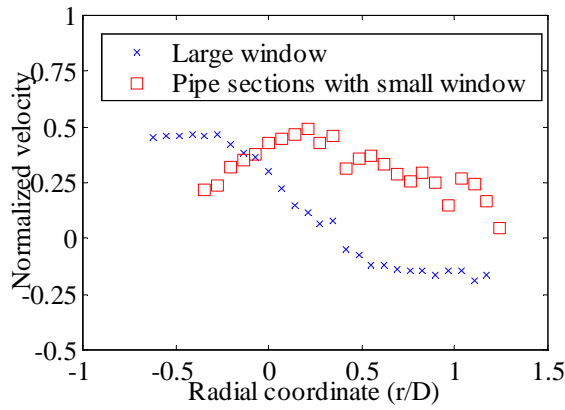


**Figure 4.28:** Flow field asymmetry at  $S=0.21$  and  $Q=50$  SCFM with and without large window

velocity distributions for  $S=0.12$  and  $S=0.16$  are virtually identical except near the profile maxima. The  $S=0.16$  case actually has a lower swirl velocity maximum than the  $S=0.12$  case, indicating a relatively rapid destruction of azimuthal momentum.

The similarities between 50 and 100 SCFM are also seen in the RMS velocity

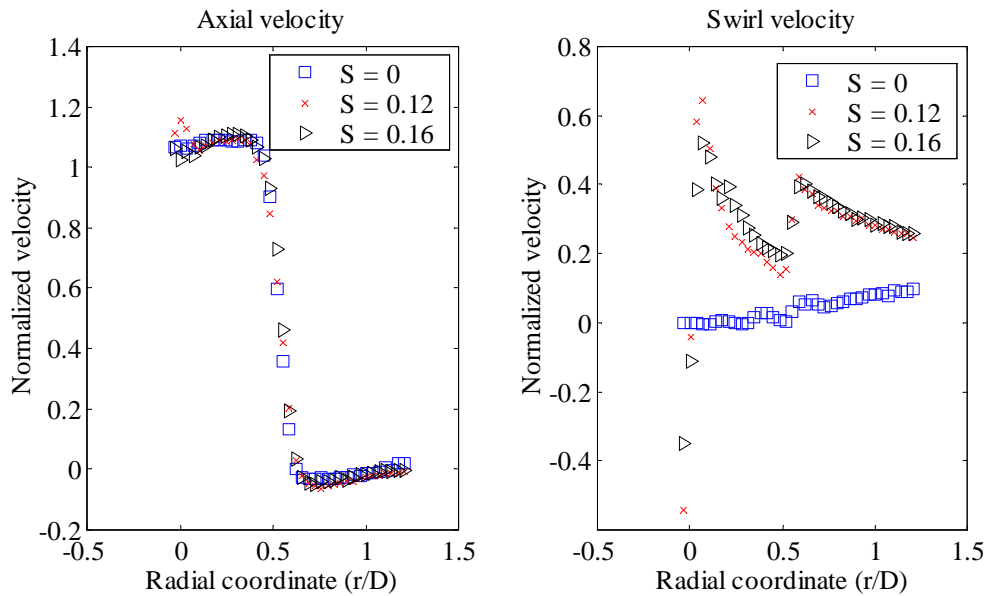


**Figure 4.29:** Comparison of combustor mean velocity profiles at all swirl levels for  $Q=100$  SCFM at  $x/D_n=0.44$

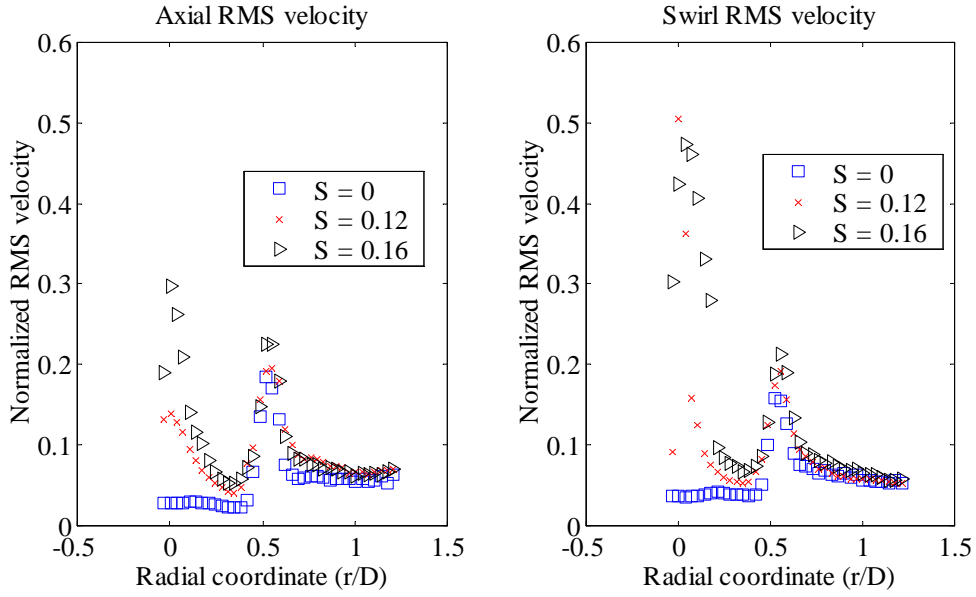


**Figure 4.30:** Comparison of combustor RMS velocity profiles at all swirl levels for  $Q=100$  SCFM at  $x/D_n=0.44$

profiles. The normalized data shown in Figure 4.30 exhibit maxima in the outer shear layer that are nearly identical in magnitude compared with the 50 SCFM case. Some differences between the two flow rates are evident near the centerline. The turbulence levels here are higher for the 100 SCFM case. It is important to remember that the maximum swirl number possible at 100 SCFM without vortex breakdown moving into the nozzle is 0.16. The centerline axial RMS velocity magnitudes for this swirl number are smaller than for the  $S=0.21$  case at 50 SCFM, but the swirl RMS velocity magnitudes at the centerline are higher than for the  $S=0.21$ , 50 SCFM case. The absence of the strong peak in axial RMS velocity for the  $S=0.16$ , 100 SCFM case is not surprising considering that the flow field does not exhibit the same strong wake flow field that is seen at the  $S=0.21$ , 50 SCFM.

The  $\overline{u'w'}$  shear stress distribution, shown in Figure 4.31 is consistent with the RMS velocity distributions. The large centerline maxima observed for the  $S=0.21$ , 50 SCFM case are absent because the  $S=0.16$ , 100 SCFM case does not exhibit the same wake type profile at the centerline. The  $\overline{u'w'}$  stress levels increase with swirl

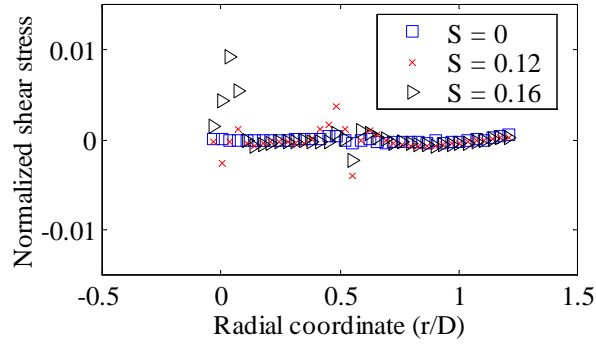


**Figure 4.31:** Comparison of combustor  $\overline{uw}$  stress at all swirl levels for  $Q=100$  SCFM at  $x/D_n=0.44$

number, consistent with the observation that the mean momentum is dissipated and redistributed more quickly at higher swirl conditions.

Figures 4.32 to 4.34 show the evolution of the flow field for the  $S=0.16$  swirl condition studied at the nominal flow rate of 100 SCFM. Although it was not very clear at  $x/D_n=0.44$  (Figure 4.29), the  $S=0.16$  case does develop a wake like profile on the centerline. The wake is most easily seen at  $x/D_n=0.97$ . It is likely that the rapid destruction of azimuthal momentum described above leads to the wake profile observed in Figure 4.32, by imposing a large adverse pressure gradient on the flow on its centerline. If the rate of destruction of azimuthal momentum for the  $S=0.16$ , 100 SCFM case is compared with the  $S=0.21$ , 50 SCFM case, it can be concluded that the rate of destruction is higher for the  $S=0.21$  case, hence leading to a greater adverse pressure gradient and a more significant wake.

The development of the flow at  $S=0.16$ , 100 SCFM follows that at  $S=0.21$ , 50 SCFM very closely. The swirl RMS velocity maximum at the centerline dissipates downstream while the RMS velocity in the outer shear layer stays nearly constant. The axial RMS velocity at the centerline increases as the outer shear layer RMS velocity maximum becomes broader.

The  $\overline{u'w'}$  shear stress distribution is also similar to the  $S=0.21$ , 50 SCFM case. A large maximum is observed near the centerline for  $x/D_n=0.97$ , when the wake is relatively strong. The magnitude of the shear stress for the  $S=0.16$ , 100 SCFM case

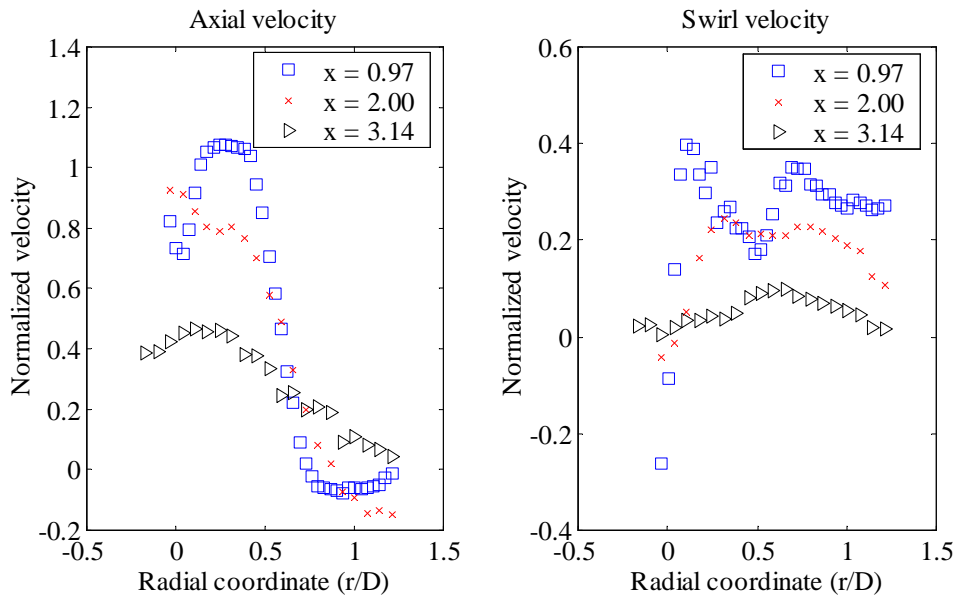


**Figure 4.32:** Evolution of combustor mean velocity for  $S=0.16$ ,  $Q=100$  SCFM

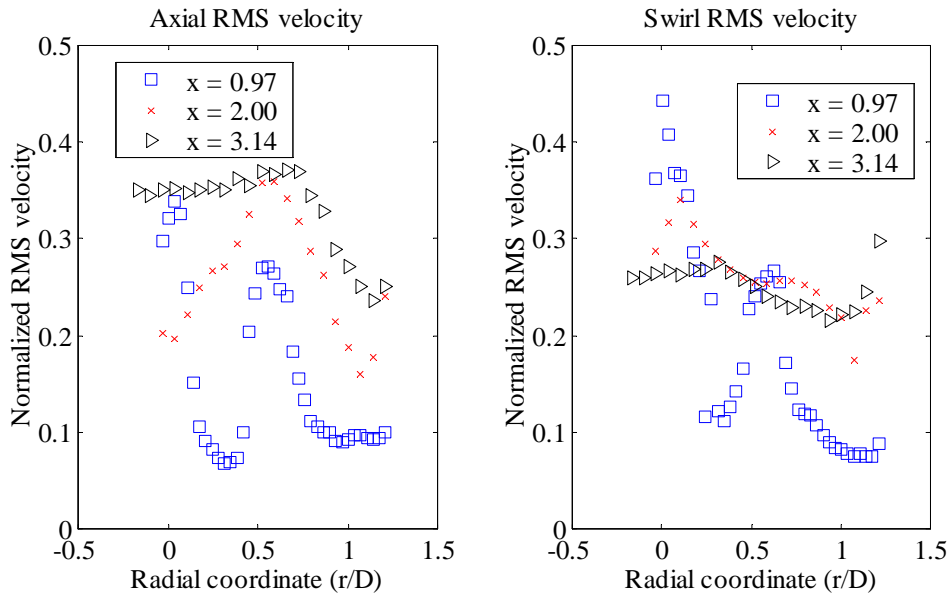


**Figure 4.33:** Evolution of combustor RMS velocity for  $S=0.16$ ,  $Q=100$  SCFM

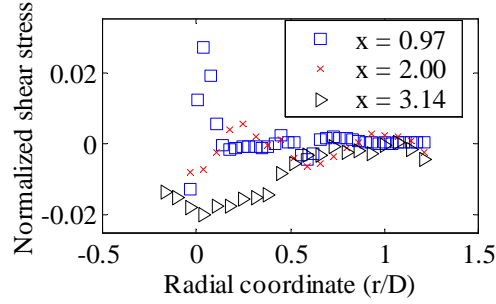


**Figure 4.34:** Evolution of combustor  $\overline{u'w'}$  stress profiles for  $S=0.16$ ,  $Q=100$  SCFM

is lower which is consistent with the fact that the wake at the centerline is weaker. At  $x/D_n=3.14$ , the  $\overline{u'w'}$  shear stress distribution does not obey the anti-symmetry requirement for axisymmetric flow. A re-examination of the mean velocity profiles does reveal a slight asymmetry at the centerline.

The strong similarities observed between the  $S=0.16$ , 100 SCFM case and the  $S=0.21$ , 50 SCFM case suggest that both cases are equally closely located in the experimental parameter space to the point where the vortex breakdown moves into the nozzle and upstream to the end of the cone center-body. Since the experimental conditions should be described fully by Reynolds number and swirl number, it is surprising that the nozzle flow loses stability at different swirl numbers for different flow rates.

In the range of Reynolds numbers studied, the flow is not expected to be very sensitive to changes in Reynolds number, and this is indeed the case for the lower swirl numbers. The dependence can therefore only be explained by the fact that an additional parameter is required to describe the experimental condition. The major difference observed in the nozzle flow field between the  $S=0.16$ , 100 SCFM case and the  $S=0.21$ , 50 SCFM case is the distribution and magnitude of the axial RMS velocity at the centerline. The cause of this difference is not known and further study is required to identify the missing experimental parameter.

As a first guess, a parameter of interest could be the following non-dimensional parameter: the vortex core diameter times the centerline slope of azimuthal velocity

divided by the average axial velocity. The parameter allows the increased centerline shear experienced for increased flow rates (with constant core size) to be accounted for. The increased shear causes increased turbulence production, in the same amount of space. The increased turbulence destabilizes the flow earlier. Experimentally, the center-body shape would have to be adjusted depending on flow rate since Garg and Leibovich (1979) found that core size is at least in part determined by the path length traveled by the inner flow over the center-body.

Another interesting characteristic of the free vortex flows studied is the distribution of swirl velocity immediately downstream of the nozzle exit. All figures showing swirl velocity profiles at  $x/D_n=0.44$  or  $x/D_n=0.97$  show a local maximum in swirl velocity just outside the outer shear layer. The increase from the inner local minimum of swirl velocity is around 20%. One possible cause for this type of profile may be the contamination of the measurements by the large radial velocities seen in this part of the flow field. However, even if the magnitude of the radial velocity were equal to that of the azimuthal velocity an incredibly large misalignment is required to cause the increase in swirl velocity seen at the boundary layer. Although not discussed, the data of Paschereit et al. (1999) exhibits a similar local maximum in swirl velocity just outside the dump in their free vortex burner model. The flow studied by Paschereit et al. (1999) is however significantly different from the present geometrical arrangement. Paschereit et al. (1999) observe a complete vortex breakdown in the center of their flow field, with reverse axial velocities in the center of the flow. The one common point is that both experiments use relatively large area expansion ratios. Other studies such as that of Ahmed (1998b) show slightly increasing swirl velocities outside the outer shear layer, but no marked local maximum such as that seen in the data here. It must be added that the experimental results using the annulus geometry do not consistently exhibit this type of swirl profile.

The case of  $S=0.12$ , 100 SCFM is not shown because its behavior is identical to the behavior of the  $S=0.12$ , 50 SCFM case.



### 4.3 Annulus geometry

Nozzle velocity profiles for the annulus nozzle geometry were measured at the same points as for the free vortex geometry. The parameters for the measurements performed for the annulus geometry are summarized in Table 4.1. Measurements inside the nozzle with the center-body present were complicated by light scattering from the center-body. To help reduce the effects of scattered light from the center-body, the center-body itself was painted black with a matte finish. Additionally, the lens was equipped with a mask that prevents a significant portion of the scattered light from being coupled into the fiber and measured by the PMT. Because of the orientation of the beams relative to the curvature of the center-body, scattered light contaminated the measurements of the azimuthal component of velocity (swirl) more readily than measurements of the axial component of velocity. Due to the influence of scattered light, data could not be taken closer than 0.12 inches from the center-body. The swirl number calculations are relatively insensitive to the lack of data close to the center-body. The most significant error is seen for the area mean velocity calculation. The values calculated are lower than what should be expected given the values for the free vortex geometry. However, the errors incurred will be similar for all cases and the value of the normalization will not be lost if the area mean velocities are calculated consistently for all the cases studied.

Due to the different reference length required for the annulus geometry, the axial and radial coordinate system will appear different, although the physical locations of measurement are the same. The nozzle velocity profiles were measured at non-dimensional axial locations of  $x/D_h=-0.53$  and  $x/D_h=-1.06$ . The non-dimensional radial coordinate ranges from  $r/D_n=0.26$  to  $r/D_n=0.76$  inside the nozzle. The downstream non-dimensional measurement locations are:  $x/D_h=0.68, 1.47, 2.26, 3.05$  and  $4.79$ . The radial coordinate range for measurements in the downstream test section is from  $r/D_n=-0.28$  to  $r/D_n=1.91$ .

### 4.3.1 Nozzle flow field

Figures 4.35 to 4.37 show the evolution of the flow field inside the nozzle at the highest swirl level studied in detail,  $S=0.60$  for the nominal flow rate of 50 SCFM. The axial velocity profile evolves little between the two measurement locations. The swirl velocity profile retains the same shape but the peak of swirl velocity decreases noticeably between measurement locations. While the swirl velocity profile looks very similar to a radially displaced free vortex profile, the axial velocity profile appears relatively flat with a slight skewness towards the outer part of the annulus. The axial momentum surplus encountered in the free vortex geometry is not seen in the annulus geometry. The favorable pressure gradient setup by the swirl distribution at the formation of the vortical flow is counter-acted in the annulus geometry by the presence of an inner wall. The losses associated with the wall do not allow the axial momentum surplus to build.

Note that the data point closest to the center-body does not fall in line with the rest of the axial velocity profile at the first axial station. Similarly, the same point in the swirl velocity profile appears to be too low. A histogram of the velocities measured here is plotted in Figure 4.38 and shows that the cause is a large peak in the distribution at zero velocity. The peak is caused by the light scattered from the center-body. Due to the proximity of the measurement volume, some very small fraction of the scattered light couples into the multi-mode fiber and appears coherent at the PMT. Note that the corresponding RMS velocity for the same data point is consequently also erroneous. The relatively close spacing of the measurement grid inside the annulus allows such bad data points to be identified relatively easily.

The RMS velocities shown in Figure 4.36, are comparable to the RMS velocities found in the free vortex geometry. The axial RMS velocities at the centerline are lower than the swirl RMS velocities. The maximum in RMS swirl velocity at the centerline is lower than the maxima seen for the free vortex geometry. The RMS distribution for both axial and swirl velocity components increases downstream. The increase is consistent with the destruction of azimuthal momentum.

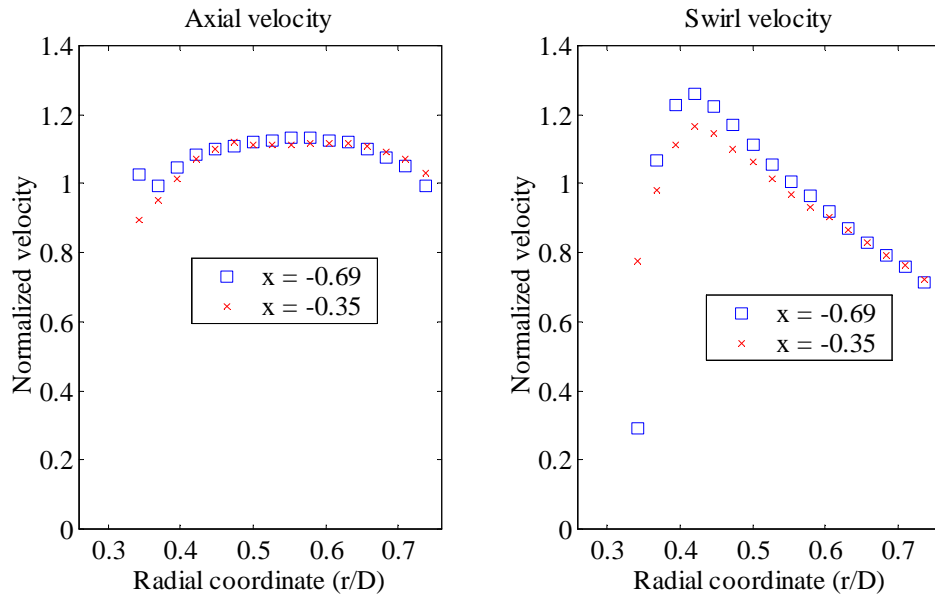


**Figure 4.35:** Comparison of nozzle mean velocity profiles at two axial locations in the annulus geometry at  $S=0.60$  and  $Q=50$  SCFM

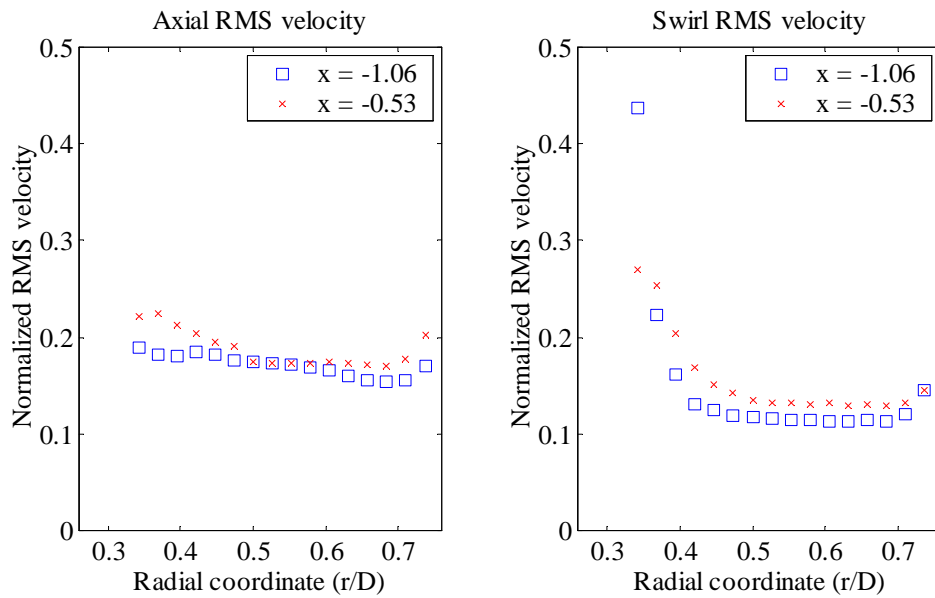


**Figure 4.36:** Comparison of nozzle RMS velocity profiles at two axial locations in the annulus geometry at  $S=0.60$  and  $Q=50$  SCFM

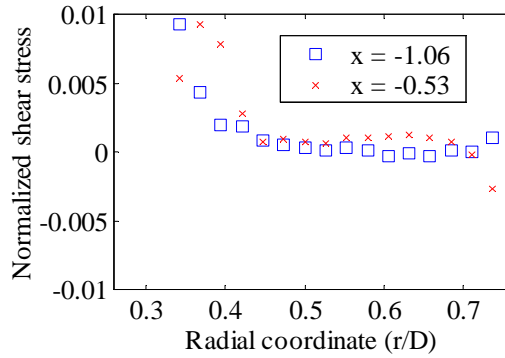


**Figure 4.37:** Comparison of nozzle  $\overline{u'w'}$  stress profiles at two axial locations in the annulus geometry at  $S=0.60$  and  $Q=50$  SCFM

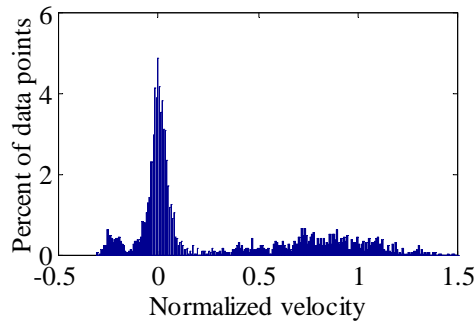


**Figure 4.38:** Histogram of swirl velocities at  $x/D_h=-1.06$ ,  $S=0.6$  and  $Q=50$  SCFM

The  $\overline{u'w'}$  shear stress distributions shown in Figure 4.37 are very similar for both axial stations. The stresses are small except near the center-body where the stresses are positive. Considering the axial dissipation of azimuthal momentum and the apparent production of turbulence, the positive stresses near the center-body should be expected. Negative axial gradients of swirl velocities together with positive  $\overline{u'w'}$  shear stress are associated with the production of turbulence.

Figures 4.39 to 4.41 compare the results at  $x/D_h=-0.53$  for all three swirl levels at 50 SCFM. Significant differences are not only seen for the swirl velocity profiles but also for the axial velocity profiles. The axial velocity profiles at zero swirl and  $S=0.28$  are very similar. Compared to these, the axial velocity at  $S=0.60$  is skewed significantly towards the outer radius. The peak in swirl velocity for the  $S=0.28$  case

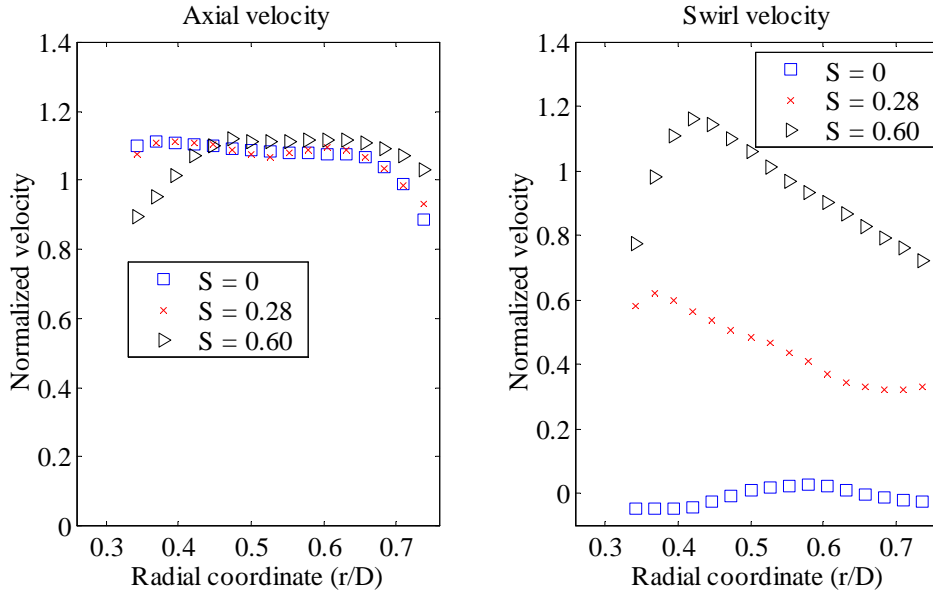


**Figure 4.39:** Comparison of nozzle mean velocity profiles for all three swirl levels at  $x/D_h = -0.53$ ,  $Q = 50$  SCFM

occurs very close to the center-body whereas at  $S = 0.60$ , the peak in swirl velocity is closer to the annulus center. Part of the velocity profile skewness at  $S = 0.6$  will be explained when the results for the downstream flow section are discussed.

The RMS velocity profiles show an increase in RMS velocity with swirl level. However, the proportionality between swirl level and RMS velocity is not direct. The difference between  $S = 0$  and  $S = 0.28$  is much smaller than the difference between  $S = 0.28$  and  $S = 0.60$ . The profiles of RMS velocity appear monotonic in the radial coordinate for  $S = 0$ , but show maxima near the center-body for  $S = 0.28$  and  $S = 0.60$ . The shear added to the flow near the center-body through the addition of swirl causes an increase in turbulence production in this area of the flow field.

The  $\overline{u'w'}$  shear stress distribution supports the conclusion of increased turbulence production near the center-body. Reasonably high positive  $\overline{u'w'}$  shear stresses are found near the wall. The distribution outside the inner region of the flow is not a strong function of swirl number.

Figures 4.42 to 4.44 compare the results at 50 and 100 SCFM for  $S = 0.28(0.29)$ .

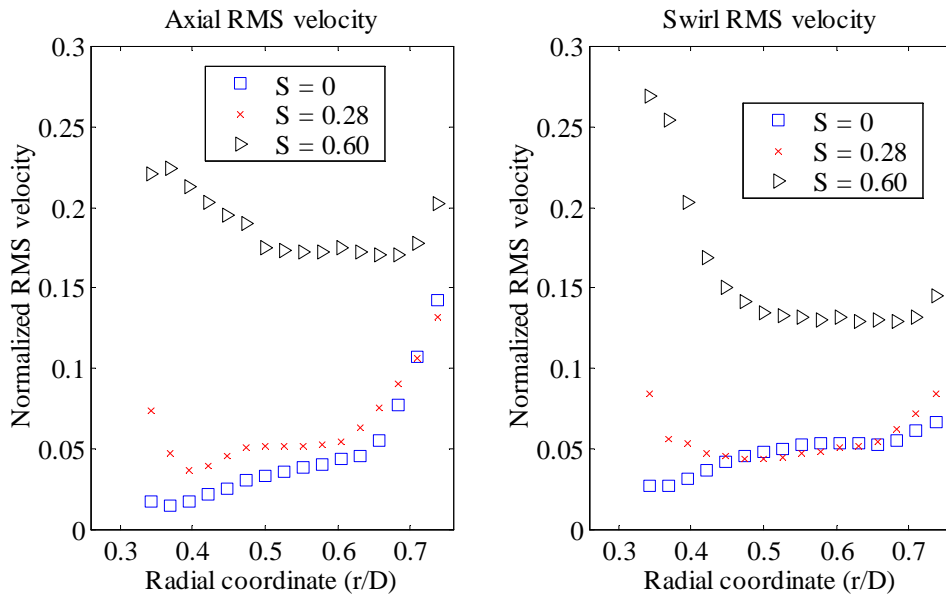


**Figure 4.40:** Comparison of nozzle RMS velocity profiles for all three swirl levels at  $x/D_h = -0.53$ ,  $Q=50$  SCFM

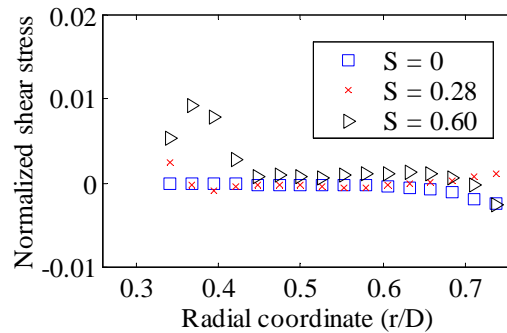


**Figure 4.41:** Comparison of nozzle  $\overline{uw}$  stress profiles for all three swirl levels at  $x/D_h = -0.53$ ,  $Q=50$  SCFM

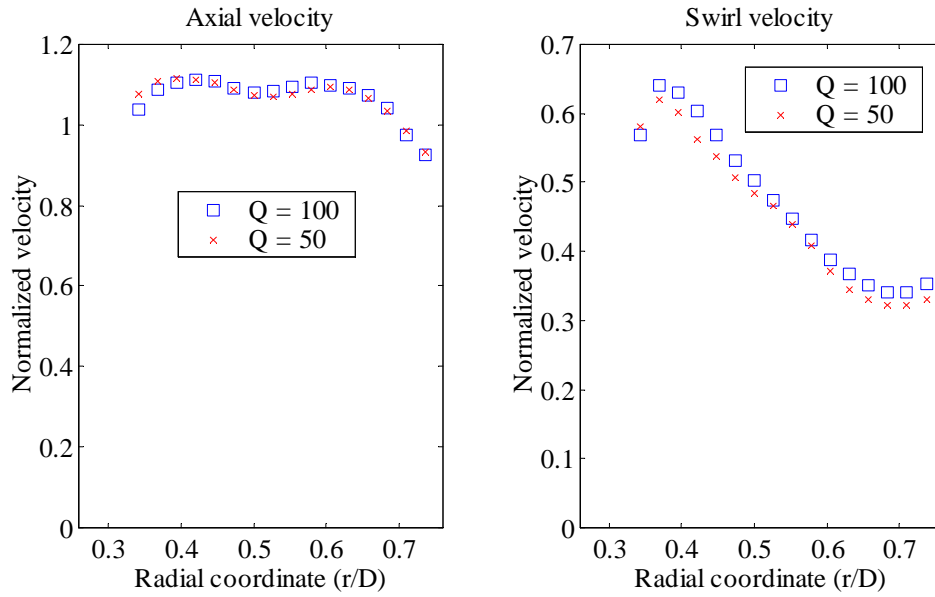


**Figure 4.42:** Comparison of nozzle mean velocity profiles in annulus geometry for two flow rates at  $S=0.28$

The mean velocity profiles extremely similar. Both axial velocity profiles show a small local minimum at the center of the annulus. The small differences observed are mostly in the swirl velocity profile. The higher flow-rate exhibits a relatively higher swirl velocity. The slightly higher swirl velocity is also reflected in the small difference in swirl numbers for the two cases. The profile shape however for both axial and swirl velocity does not change with flow rate.

Larger differences can be seen in the RMS velocity distributions. The differences between the RMS velocity distributions are confined to inner parts of the flow. Toward the outer wall, the results from both flow rates collapse to the same curve. For both axial and swirl RMS velocity profiles, the RMS velocities at  $Q=100$  SCFM lie above the RMS velocities at  $Q=50$  SCFM. Both RMS velocity distributions exhibit a bucket shape that is expected due to turbulence production in the inner and outer parts of the flow. Compared with the  $S=0.6$  case, it appears the turbulence production is more balanced for the  $S=0.28$  case.

The relatively flow-rate independent results are also seen in the  $\overline{u'w'}$  stress distribution. Shallow maxima are seen near the center-body, indicating the swirl induced

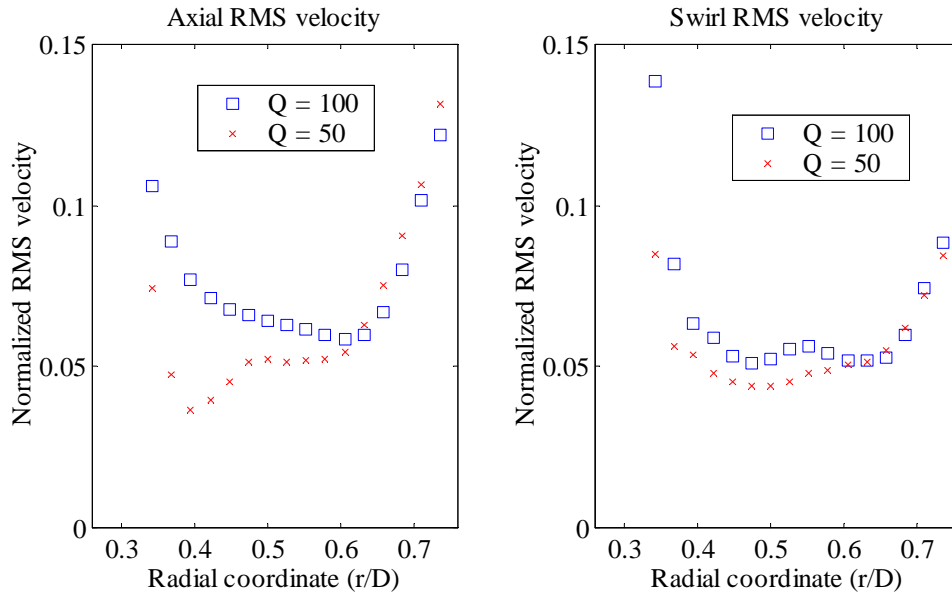


**Figure 4.43:** Comparison of nozzle RMS velocity profiles in annulus geometry for two flow rates at  $S=0.28$

production of turbulence, observed previously. The stress levels overall are low due to the relative isotropy that exists in the flow.

### 4.3.2 Post sudden expansion flow field

Figures 4.45 to 4.47 compare the characteristics of the flow fields for all three swirl conditions immediately after the flow enters the downstream test section ( $x=0.68$ ) at

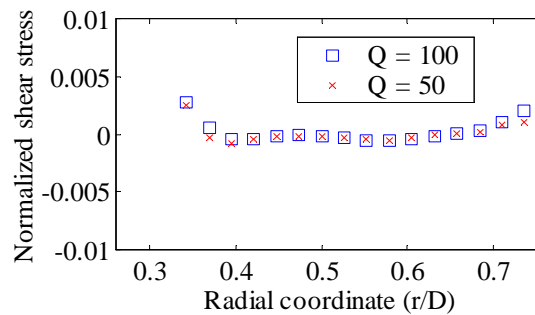


**Figure 4.44:** Comparison of nozzle  $\overline{uw}$  stress profiles in annulus geometry for two flow rates at  $S=0.28$



a nominal flow rate of 50 SCFM. Three very different flow fields can be identified from the plots. At the largest swirl number, a wide recirculation region has formed behind the center-body. Without swirl a small narrower recirculation zone is observed behind the center-body. The  $S=0.28$  condition does not show reversed flow on a time average basis behind the center-body. For the  $S=0.60$  case, the wide recirculation zone appears to have pushed the incoming axial momentum and azimuthal momentum towards the outside of the flow field. The large flow divergence observed for  $S=0.60$  may be partly responsible for the distribution of axial momentum in the nozzle discussed above. The swirl velocity profile for  $S=0.60$  case has a single maximum and decays slowly throughout the outer part of the flow field. The inner distribution is largely linear indicating solid body rotation.

The slowly decaying swirl velocity in the outer part of the flow field matches the  $S=0.28$  swirl velocity distribution very closely. The  $S=0.28$  swirl velocity distribution is however very different. The distribution is narrower with the maximum occurring well within the  $S=0.60$  maximum. Additionally, a local maximum is observed in the swirl velocity profile, similar to the free vortex profiles discussed above. The fact that the  $S=0.60$  case does not exhibit the secondary maximum, even though this case arguably has the larger radial velocity supports the claim made above that the secondary maximum again observed here for the  $S=0.28$  case is not due to a misalignment measurement error.

The axial velocity distribution does not only exhibit major differences in the amount and size of recirculation depending on the swirl number. The behavior outside the recirculation zone also strongly depends on the swirl number. For the  $S=0.6$  case a very narrow annular jet is produced whose velocity maximum is displaced to the location of the outer shear layer of the entering flow. The shear layer can be easily identified in the  $S=0$  and  $S=0.28$  flow fields. The flat axial velocity profiles measured in the nozzle for these cases can still be identified at this axial location, downstream of the expansion.

It is also possible to identify a small non-zero swirl distribution for  $S=0$  in Figure 4.45. This distribution is inherited from the nozzle where it can also be identified.

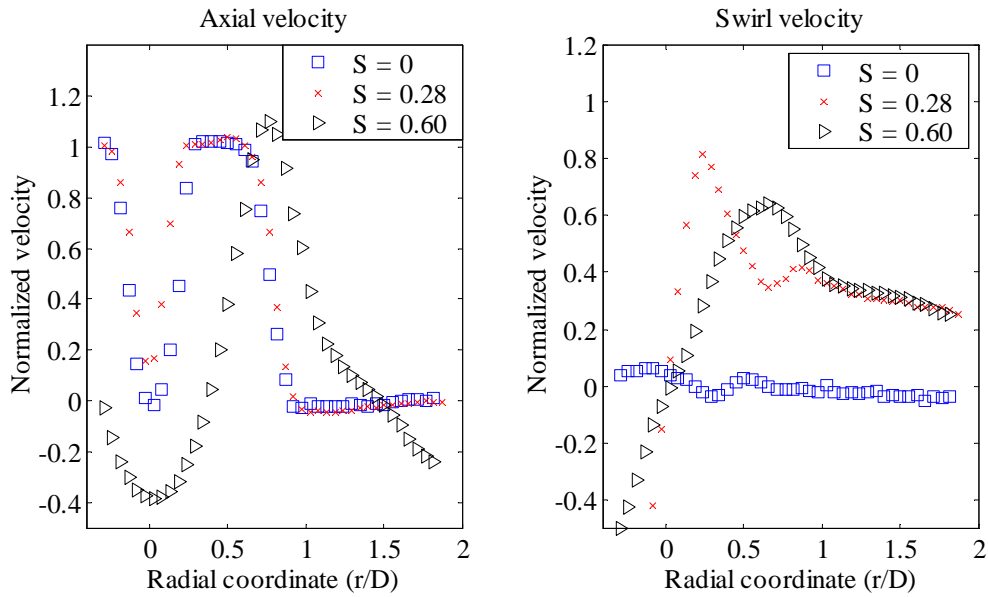


**Figure 4.45:** Comparison of combustor mean velocity profiles in annulus geometry for all swirl conditions at  $x/D_h=0.68$ ,  $Q=50$  SCFM

The cause of the uneven swirl distribution is imperfect alignment of the swirl vanes. The accuracy of aligning all eight swirl vanes to the same angle was limited to that achievable using the fine tooth gears employed in the present study. The slight rotational errors cause small vortices to form and travel down the nozzle at off center locations. At any angle other than zero degrees these vortices organize themselves into the prevailing swirl momentum distribution and do not survive into the nozzle.

The RMS velocity distributions are shown in Figure 4.46. The RMS velocity distributions reveal many interesting flow features. The wake of the center-body clearly represents another shear layer which will cause significant turbulence production. The distribution of maxima and minima of RMS velocity in the center-body wake strongly depends on the swirl number but in general, a minimum of axial RMS velocity is observed at the centerline whereas a maximum in swirl RMS velocity is observed here. Even the case of  $S=0.28$  exhibits a small local minimum at the centerline. The width of the local minimum in axial RMS velocity corresponds closely with the width of the maximum in the swirl RMS velocity distribution. The inner

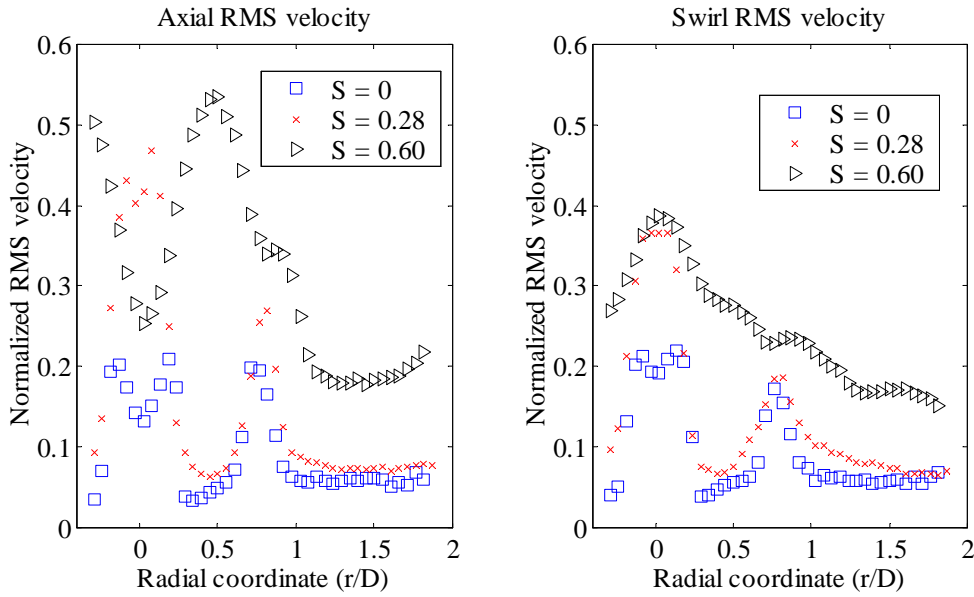


**Figure 4.46:** Comparison of combustor RMS velocity profiles in annulus geometry for all swirl conditions at  $x/D_h=0.68$ ,  $Q=50$  SCFM

shear layer produces both the swirl and axial RMS velocity maxima. This stands in contrast to the free vortex case where the inner shear layer produced the swirl RMS velocity maximum whereas the outer shear layer produced the axial RMS velocity maximum. Secondary maxima can be observed for all swirl strengths in the outside shear layer. The maximum is weakest for the  $S=0.6$  case where it is almost swallowed by the width of the RMS velocity maximum stemming from the inner shear layer.

The large differences observed between the axial and swirl RMS velocity distributions indicate a large amount of anisotropy and associated turbulence production in the flow. The  $\overline{u'w'}$  shear stress profiles shown in Figure 4.47 are consistent with the RMS velocity distributions just described and exhibit very clear antisymmetry about the centerline, as expected. The axisymmetric flow conditions implied by the measured  $\overline{u'w'}$  stress distribution, shows that whatever unsteady motions may be present, the underlying mean flow distribution is axisymmetric. Thus note that the shear stress is almost non-existent for the zero swirl case as expected.

The development of the flow field beyond the sudden expansion for the case

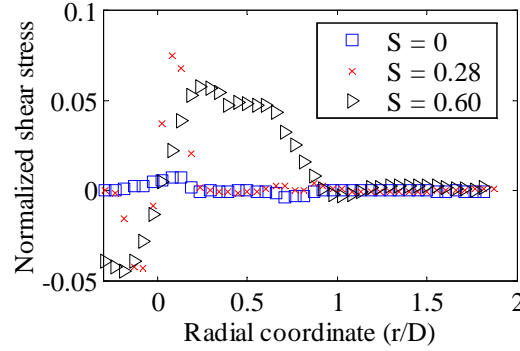


**Figure 4.47:** Comparison of combustor  $\overline{u'w'}$  stress distributions in annulus geometry for all swirl conditions at  $x/D_h=0.68$ ,  $Q=50$  SCFM

of  $S=0$  at a flow rate of 50 SCFM is shown in Figures 4.48 to 4.50. The small reversed flow region in the wake of the center-body recovers quickly downstream and at  $x/D_h=4.79$ , no axial velocity deficit can be distinguished on the centerline. The overall magnitude of the axial velocity has however barely decayed and the flow at  $x/D_h=4.79$  resembles that of a jet whose potential core is still intact. In the outer region of the flow, reverse flow develops as the flow evolves downstream, and is still present at  $x/D_h=4.79$ . The small non-zero swirl velocities observed upstream at  $x/D_h=0.68$  can still be seen at the downstream measurement locations although the magnitude of the velocities is slowly decaying.

The axial RMS velocity distribution shown in Figure 4.49 changes significantly as the flow moves downstream. The maxima in RMS velocity stemming from the inner shear layer decay until at  $x/D_h=0.68$ , a wide local minimum is observed at the center of the flow field, a condition consistent with the jet like mean axial velocity distribution. The swirl RMS velocities are lower than the axial RMS velocities but mirror the development of the axial RMS velocity.

The  $\overline{u'w'}$  shear stress distribution shown in Figure 4.50 does not exhibit any large deviations from zero, as expected for an axisymmetric flow with no swirl. The distributions do exhibit small non-zero stress values at the centerline, which would normally indicate some degree of circumferential asymmetry. However, the magnitudes are so small that concerns about asymmetry must be dismissed as the non-zero

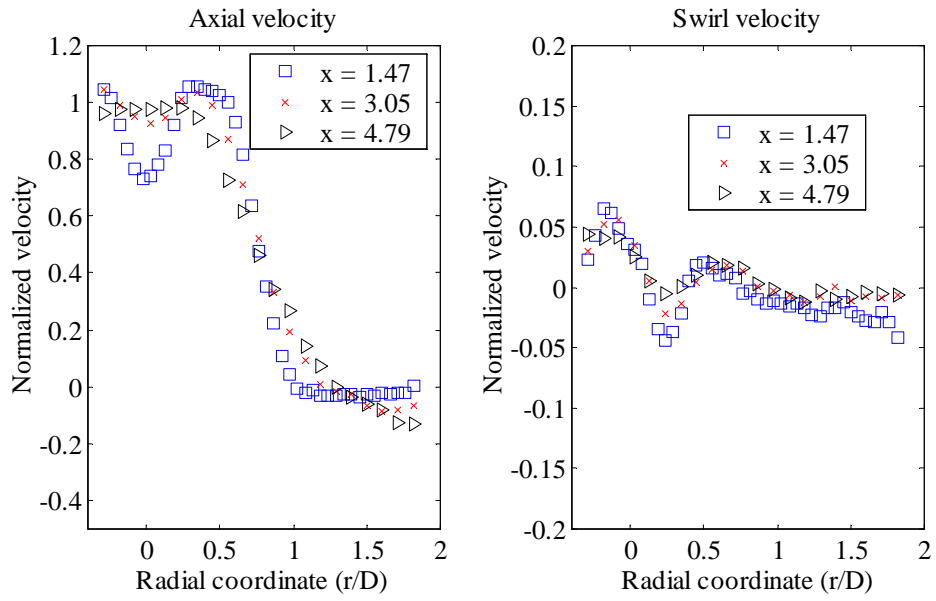


**Figure 4.48:** Evolution of combustor mean velocity profiles in annulus geometry for  $S=0$ ,  $Q=50$  SCFM

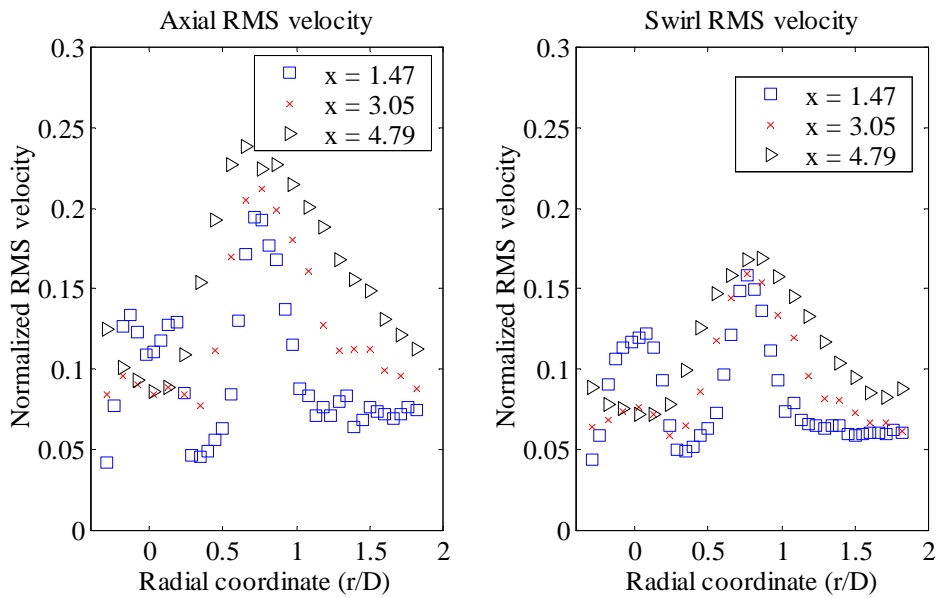


**Figure 4.49:** Evolution of combustor RMS velocity profiles in annulus geometry for  $S=0$ ,  $Q=50$  SCFM

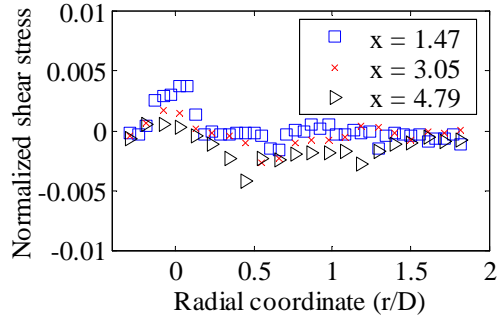


**Figure 4.50:** Evolution of combustor  $\overline{u'w'}$  stress profiles in annulus geometry for  $S=0$ ,  $Q=50$  SCFM

values are likely the result of an insufficient number of data points being collected to resolve the true, zero stress distribution expected.

The evolution of the flow field for  $S=0.28$  and a flow rate of 50 SCFM is described by Figures 4.51 through 4.54. The wake observed at the first axial station for this swirl condition persists to  $x/D_h=1.47$  and then is rapidly dissipated so that already at  $x/D_h=3.05$ , the maximum velocity in the measurement domain is located at the centerline of the test section. The rapid development of the axial velocity is likely closely related to the equally fast dissipation of azimuthal momentum between  $x/D_h=1.47$  and  $x/D_h=3.05$ . A similarly fast wake recovery was observed in Figure 4.25. The dissipation of azimuthal momentum is associated with the rapid production of turbulence which in turn enhances mixing and allows the flow to redevelop more quickly. The relatively small vortex core seen in the flow at  $x/D_h=1.47$  expands rapidly downstream. The mean swirl velocity distribution resembles that of a very broad solid body rotation flow by  $x/D_h=3.05$ .

The RMS velocity distributions shown in Figure 4.52 exhibit a very complex structure. The axial RMS velocity distribution has maxima associated with the wake shear layer in addition to the outer shear layer related maximum. The center of the wake, as already seen in Figure 4.45 has a local minimum in axial RMS velocity and a maximum in swirl RMS velocity. Similar to the free vortex case, swirl RMS velocity in the outer shear layer does not increase significantly downstream. In the

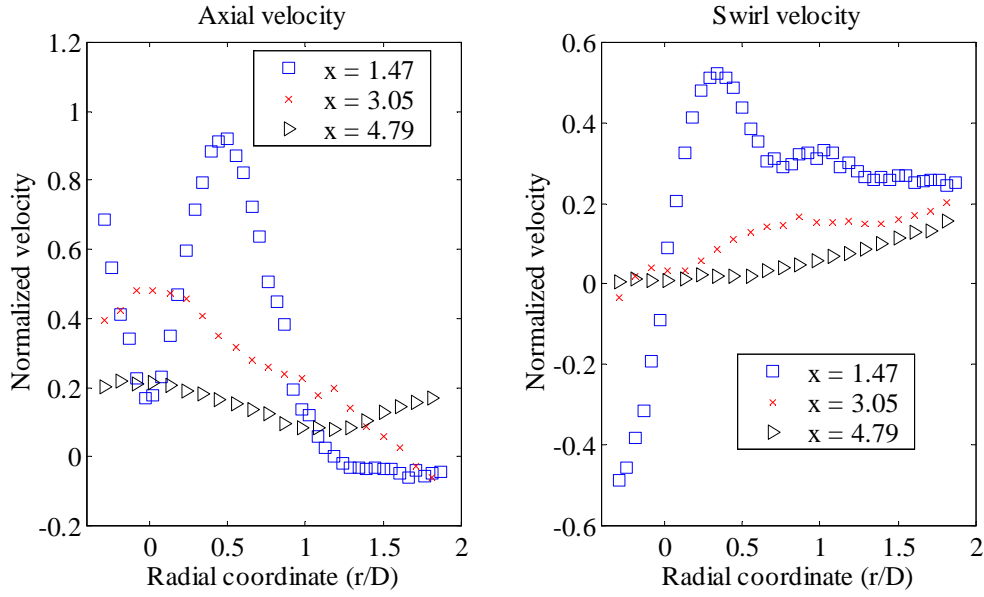


**Figure 4.51:** Evolution of combustor mean velocity profiles in annulus geometry for  $S=0.28$ ,  $Q=50$  SCFM

free vortex case however, the significant decrease in swirl RMS velocity seen between  $x/D_h=3.05$  and  $x/D_h=4.79$  was not measured. Overall the RMS velocity level has dropped significantly by the time the flow reaches  $x/D_h=4.79$ . However, relative to the local mean velocity, the fluctuations are extremely high. The mean axial velocities at  $x/D_h=4.79$  average around 0.20, meaning that nearly the entire flow field has a standard deviation equal to its mean velocity. Intermittent flow reversal thus occurs over the entire cross-section. The dynamics of the flow field will be examined in detail Chapter 5.

Figures 4.53 and 4.54 show the distribution of the  $\overline{u'w'}$  turbulent shear stress. Figure 4.54 has decreased y-axis limits to allow the distribution to be examined in greater detail. The large peaks shown in Figure 4.53 are associated with the wake and point to the significant anisotropy of the flow field and associated turbulence production and redistribution of mean momentum. Figure 4.54 shows the outer distribution of the  $\overline{u'w'}$  shear stress more clearly. The  $\overline{u'w'}$  shear stress also shows small deflections from zero in the region of the outer shear layer, as expected. The  $\overline{u'w'}$  shear stress at  $x/D_h=4.79$  is low throughout the flow field which is consistent with

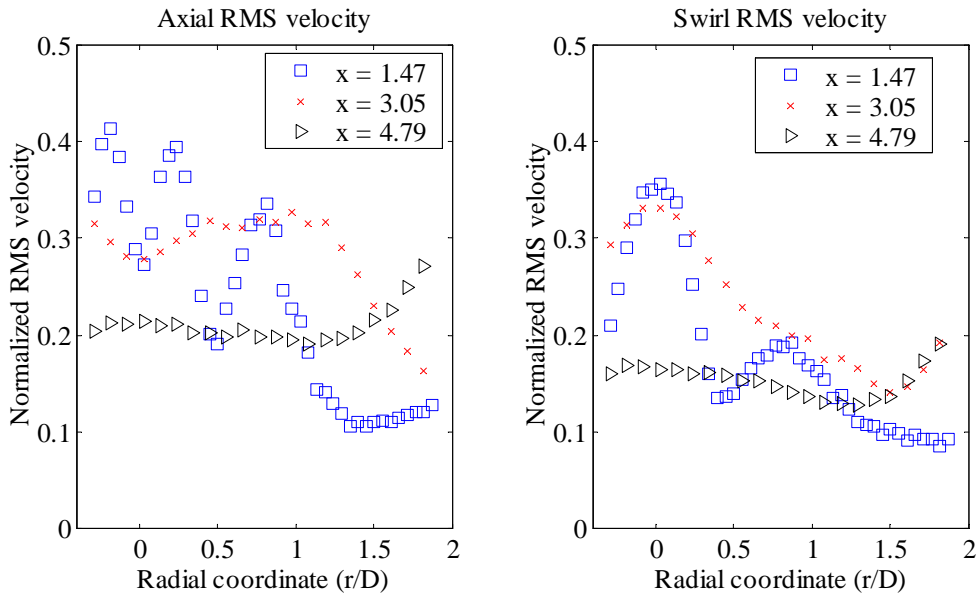


**Figure 4.52:** Evolution of combustor RMS velocity profiles in annulus geometry for  $S=0.28$ ,  $Q=50$  SCFM

a turbulent state that based on the distributions in Figure 4.52 is relatively close to isotropic. Note that all data presented obeys the antisymmetry requirement for the  $\overline{u'w'}$  shear stress.

One of the more interesting features of the evolving flow field is the local axial velocity minimum that has developed at  $x/D_h=4.79$ . These measurements were repeated to ensure that the results could be trusted and each time the results were the

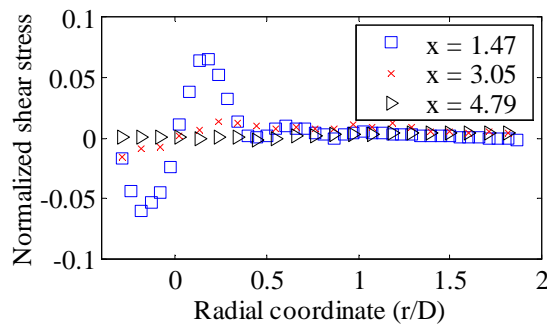


**Figure 4.53:** Evolution of combustor  $\overline{u'w'}$  stress profiles in annulus geometry for  $S=0.28$ ,  $Q=50$  SCFM



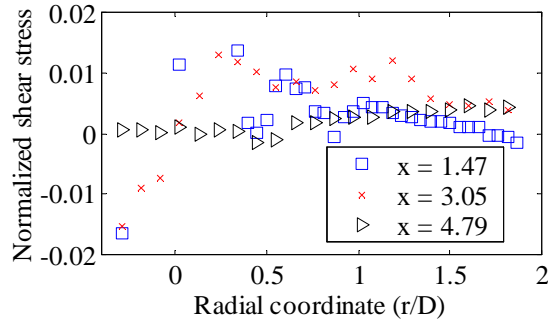


**Figure 4.54:** Evolution of combustor  $\overline{u'w'}$  stress profiles in annulus geometry for  $S=0.28$ ,  $Q=50$  SCFM (zoom to  $\pm 0.02$ )

same. Additionally, data was taken at  $x/D_h=4.0$ . The results for the mean axial velocity are shown in Figure 4.55. The figure clearly shows that the wake seen at  $x/D_h=4.79$  is starting to develop at  $x/D_h=4.0$ . The origin of the wake appears to be in the outer separation zone of the flow, which at  $x/D_h=4.0$  no longer exhibits reverse flow but influences the redevelopment of the flow downstream. The flow structure observed here was not seen for the free vortex geometry since that flow (under any of the studied swirl strengths) never redeveloped to the point where no reverse flow occurred in the outer flow field.

These results also support the change in reference lengths between the free vortex geometry and the present annulus geometry. The flow field measurements at  $x/D_h=3.05$  compare much better to the  $x/D_h=3.14$  free vortex geometry measurements than the  $x/D_h=4.79$  measurements which are taken at the same physical location.

Figures 4.56 to 4.58 show the evolution of the flow field at  $S=0.60$  at a flow rate of 50 SCFM. The wide wake observed in Figure 4.45 for  $S=0.60$  can still be easily identified in Figure 4.56. In the outer region of the flow a second significant recirculation region has also developed. The recirculation closes quickly and at  $x/D_h=3.05$ , a wall jet has developed with the bulk of the forward flow occurring near the outside walls. Detailed measurements were performed to attempt to resolve the steep profiles next to the test section wall. The reverse flow region at the centerline of the flow slowly

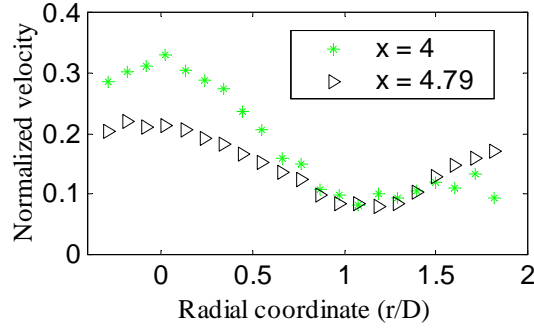


**Figure 4.55:** Comparison of axial velocity profiles at  $x/D_h=4$  and  $x/D_h=4.79$  for  $S=0.28$ ,  $Q=50$  SCFM

closes but time mean reverse flow still exists at  $x/D_h=4.79$ . The mean swirl velocity does not decay nearly as rapidly as observed for the  $S=0.28$  case. Throughout the measured flow field, a clear vortex with solid body swirl rotation can be observed in the flow. The swirl velocity profile evolves from that of a free vortex type to that of a forced vortex type as might be expected from an axial swirler. A significant amount of azimuthal momentum persists to the last measured axial location, contrary to all other measurement results presented thus far. One of the possible reasons why the azimuthal momentum is not converted to turbulent energy is the lack of a free shear layer with significant mean shear. The velocity profiles at  $x/D_h=3.05$  and  $x/D_h=4.79$  appear as very wide wakes in the center of the flow. The outer steep shear layer produces some turbulence, but the proximity of the wall also causes significant dissipation.

The most significant dissipation of azimuthal momentum occurs from  $x/D_h=1.47$  to  $x/D_h=3.05$  under the action of the significant shear that still exists in the flow at  $x/D_h=1.47$ . Between  $x/D_h=3.05$  and  $x/D_h=4.79$  however, little mean shear exists in the flow and little dissipation of azimuthal momentum is observed. Figure 4.57 shows RMS velocity distributions. The RMS velocities decline sharply between  $x/D_h=1.47$  and 3.05. The decline parallels the mean axial velocity development. With significant shear present in the mean flow at  $x/D_h=1.47$ , large RMS velocities are observed. The maxima in RMS velocity are however not lined up with the point of maximum shear.

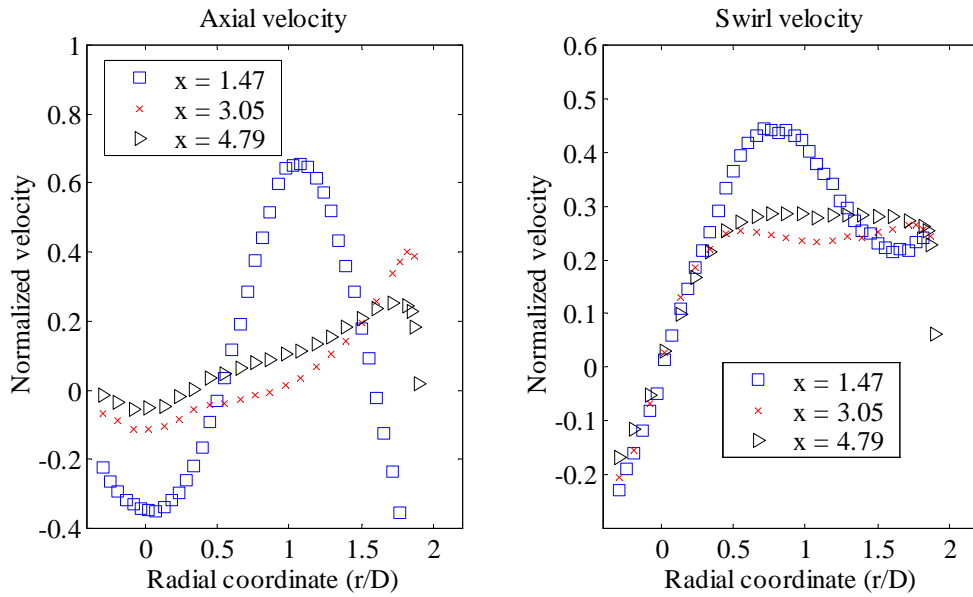


**Figure 4.56:** Evolution of combustor mean velocity profiles in annulus geometry for  $S=0.60$ ,  $Q=50$  SCFM

The local maximum observed in the center of the wake for the swirl RMS velocity profile at  $S=0.28$  is absent here. Both axial and swirl RMS velocity distributions exhibit peaks at the same radial locations. The turbulence distribution is however not isotropic because the axial RMS velocity maximum is much higher than the swirl RMS velocity maximum. At  $x/D_h=3.05$  and  $x/D_h=4.79$  little mean shear is present (especially in the axial velocity profile) and the RMS velocities are lower. The decline is slowest in the outer region of the flow field, where the most significant mean axial velocity shear is found.

The  $\overline{u'w'}$  shear stress distribution shown in Figure 4.58 reflects the relative inactivity in the flow beyond  $x/D_h=3.05$ . Significant shear stresses are present at  $x/D_h=1.47$  only. It is between  $x/D_h=1.47$  and  $3.05$  that the significant redistribution of axial momentum occurs.

One of the most important aspects to note in comparing the flow development at  $S=0.60$  to the development at  $S=0.28$  is the large difference in turbulent energy present at the last measured axial station. The turbulence at  $S=0.28$  is almost dou-

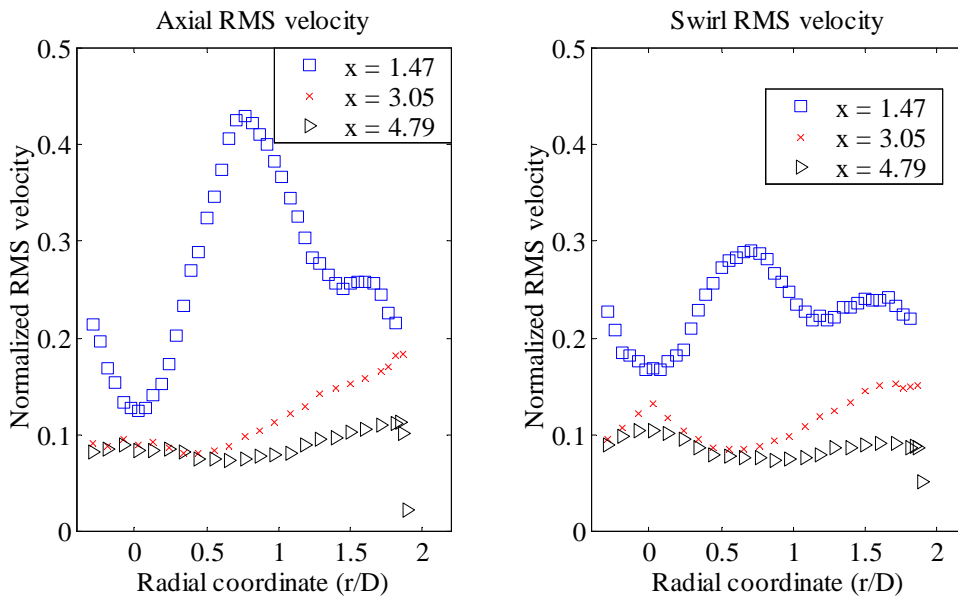


**Figure 4.57:** Evolution of combustor RMS velocity profiles in annulus geometry for  $S=0.60$ ,  $Q=50$  SCFM

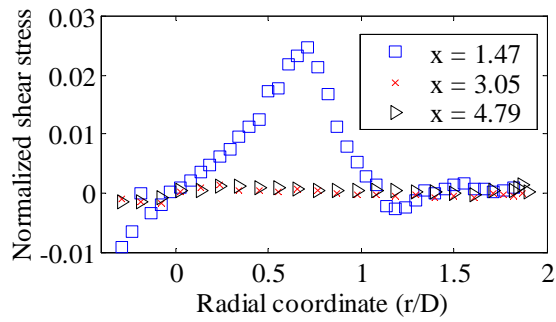


**Figure 4.58:** Evolution of combustor  $\overline{u'w'}$  stress profiles in annulus geometry for  $S=0.60$ ,  $Q=50$  SCFM

ble that at  $S=0.60$ . From an applications standpoint, this is very important. The reduced turbulence downstream mean reduced mixing of cooling flows with primary zone gases. In some sense the lower swirl number operating condition may thus be considered preferable to the higher swirl number condition. Another view of this is that only the higher swirl number flow field exhibits the rapid flow development required for a compact combustor. In the design of a flow field however turbulence longevity may be as important as turbulence magnitude for overall mixing efficiency.

The development of the flow field at 100 SCFM follows that at 50 SCFM without exception. The qualitative and quantitative similarity between the mean and RMS velocity distributions is remarkable. The following figures summarize the similarity by showing selected snapshots of the similarity rather than an exhaustive series of figures. The foci of comparison will be the two axial measurement locations of  $x/D_h=1.47$  and  $x/D_h=3.05$ . Figure 4.59 compares mean velocity profiles at  $S=0.6$  and  $x/D_h=1.47$ . Figure 4.60 shows a comparison of RMS velocity profiles for the same conditions. Figure 4.61 compares the mean velocity profiles at the same swirl number and  $x/D_h=3.05$ . Figure 4.62 compares mean velocity profiles at  $x/D_h=1.47$  for  $S=0.28$ . Finally, Figure 4.63 compares the axial mean and RMS velocity profiles for  $S=0$  at  $x/D_h=3.05$ .

The only place where somewhat large deviations between the two flow rates can be seen is in the RMS velocity distributions shown in Figure 4.60. The axial and swirl RMS velocity profiles shown have the same shape regardless of the flow rate but the magnitudes are somewhat lower for the 50 SCFM case. Given that complete similarity of the flow field is maintained (see Figure 4.61), the differences in the distributions do not appear to contribute significantly to the further development of the flow field.

The similarity between the high and low flow rate cases highlights a major difference between the free vortex geometry and the annulus geometry. The annulus geometry experimental results appear to be described completely by the swirl number of the flow alone. Realizing that both flow rates are in the turbulent range of Reynolds numbers a lack of sensitivity to this parameter may be expected. However, the similarity over a doubling of the parameter in question is still remarkable.

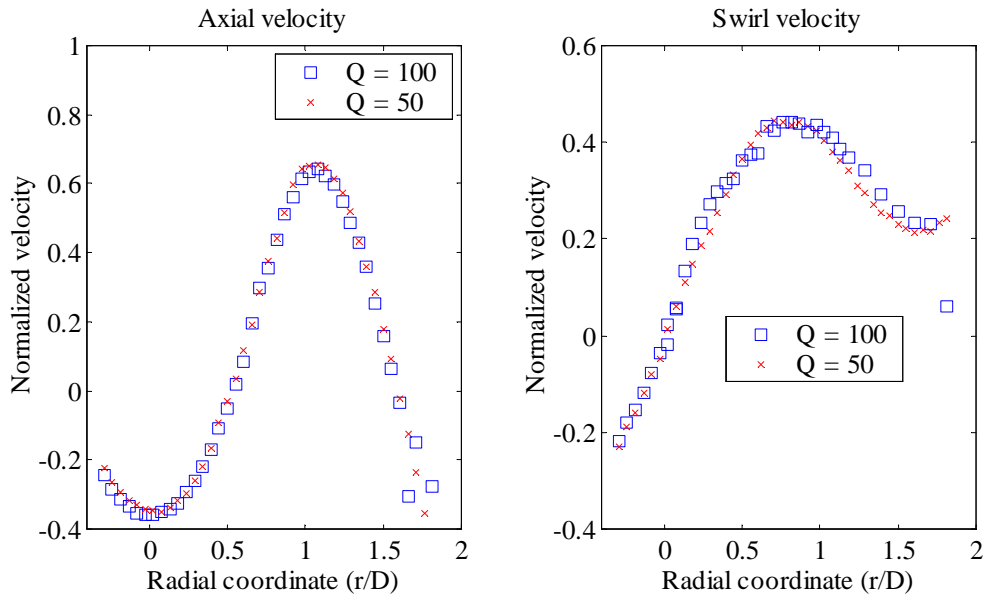


**Figure 4.59:** Flow rate comparison:  $S=0.60$  and  $x/D_h=1.47$  - Mean axial and swirl velocity

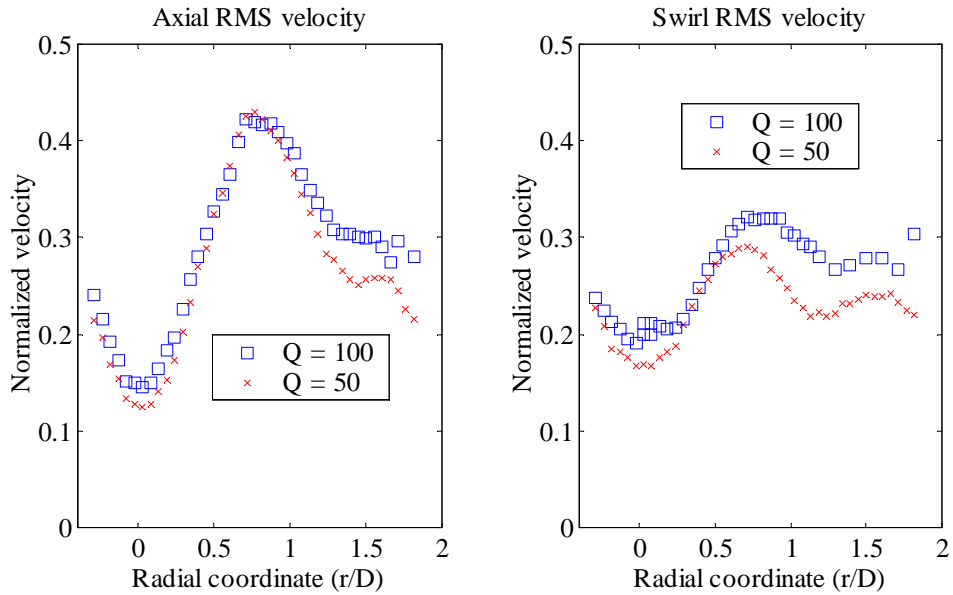


**Figure 4.60:** Flow rate comparison:  $S=0.60$  and  $x/D_h=1.47$  - Axial and swirl RMS velocity

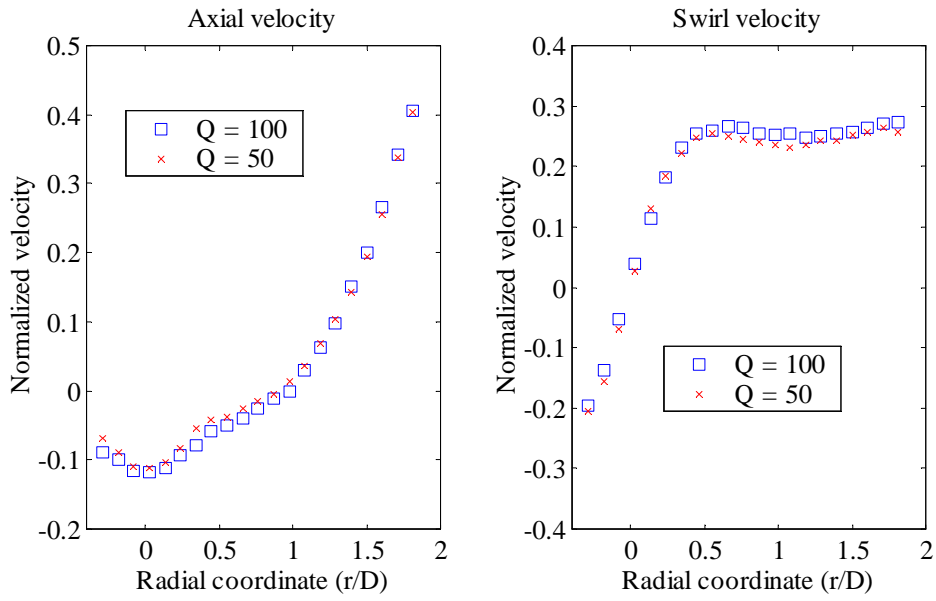


**Figure 4.61:** Flow rate comparison:  $S=0.60$  and  $x/D_h=3.05$  - Mean axial and swirl velocity

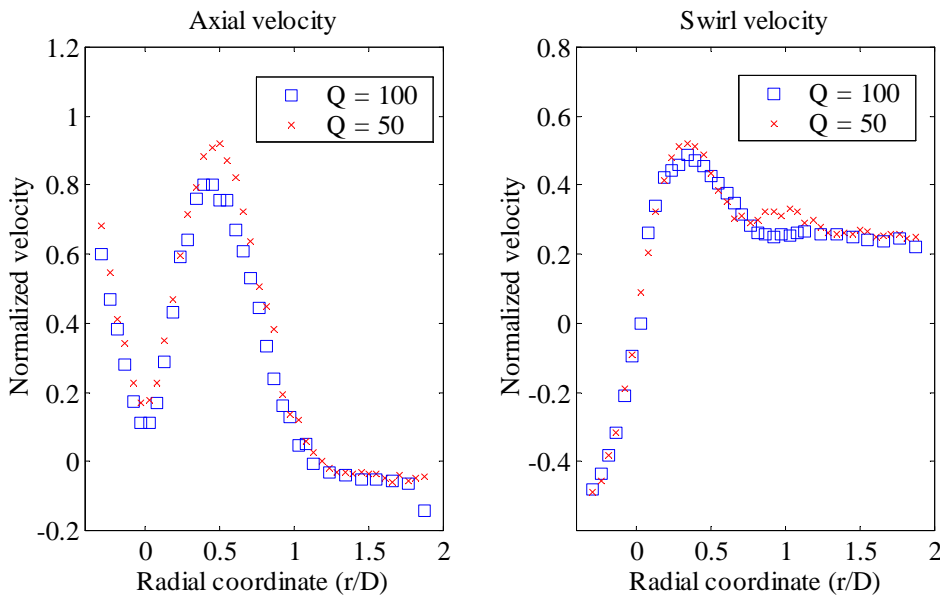


**Figure 4.62:** Flow rate comparison:  $S=0.28$  and  $x/D_h=1.47$  - Mean axial and swirl velocity

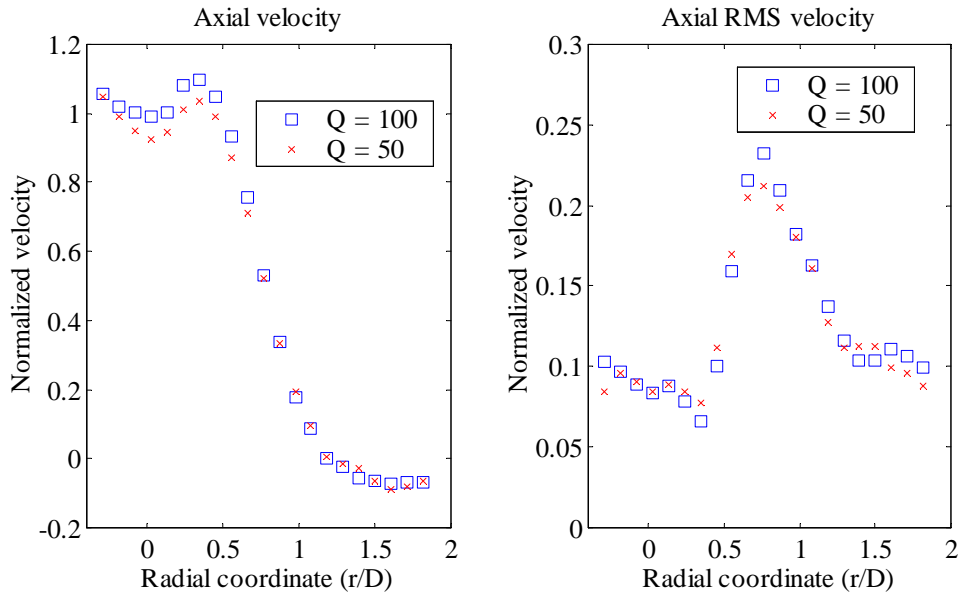


**Figure 4.63:** Flow rate comparison:  $S=0$  and  $x/D_h=3.06$  - Axial mean and RMS velocity

Eventually, higher Reynolds numbers can be expected to introduce a large enough difference in turbulence scales that noticeable differences in the flow development are caused.

Finally, none of the velocity distributions shown downstream of the sudden expansion for the annulus geometry exhibit any noticeable asymmetry. The most sensitive parameter to asymmetry is the  $\overline{u'w'}$  turbulent shear stress. In all annulus geometry cases, where significant  $\overline{u'w'}$  shear stresses were measured, the stress distribution was anti-symmetric about the flow centerline, as expected for an axisymmetric flow field. Flow field asymmetry is thus confined to the free vortex geometry and is therefore unlikely to be directly related to the experimental configuration of the downstream section. It is of course possible that the free vortex geometry is especially sensitive to the smallest rig asymmetries because the configuration allows the center of the flow to "wander" into the sudden expansion slightly off-center.

The only swirl condition studied with significant reverse flow is the  $S=0.60$  case in the annular geometry. The angle of the swirl helix (as measured by Garg and Leibovich (1979)) for this case is 50 degrees, an angle associated with the bubble type



of vortex breakdown in the study of Garg and Leibovich (1979). All other conditions exhibit maximum swirl angles lower than 45 degrees and so if breakdown is observed, it is expected to be of the spiral type and the reverse flow region is expected to be weaker. The weaker wake type flows observed may be representative of the spiral form of vortex breakdown.